GAMMAS 2026, Vol. 8, No. 1, p. 38–52 DOI: 10.14464/gammas.v8i1.966

International Association
of Applied Mathematics and Mechanics
– Archive for Students –

Simulation of a Falling Elastic Ball using ALE-Fluid-Structure-Interaction with Finite Elements

Florian Stahlhuth[a,b,⋆], Chiara Hergl[a,b], Thomas Wick[a,b]

[a] Institute for Applied Mathematics, Leibniz University Hannover, Welfengarten 1, Hannover, 30167, Germany
[b] International Research Training Group (IRTG) 2657, Leibniz University Hannover, Appelstrasse 11/11a, Hannover, 30167, Germany

received 01.04.2026, accepted 05.06.2026, published 30.06.2026

⋆ corresponding author: florian.stahlhuth@stud.uni-hannover.de

Abstract: *In this work, we show the viability of an Arbitrary Lagrangian Eulerian approach in a large deformation setting with contact by applying it to the example of a falling elastic ball. In the presented method the mesh motion is realized by solving an additional nonlinear harmonic equation, whereas discretization is achieved by finite differences in time and by a Galerkin finite element method in space. The resulting system of nonlinear equations is solved by application of a Newton-like method. In a computational analysis with two parameter sets, we investigate the behavior of the elastic ball for different mesh refinements and time step sizes. Our results show the ALE method with proper choices of mesh refinement and time step size is indeed capable of simulating the falling elastic ball. Moreover, it provides results that are overall comparable to a fully Eulerian approach.*

Keywords: Finite Element Method, Fluid-Structure Interaction, Arbitrary Lagrangian Eulerian, Falling Ball in Viscous Fluid

1 Introduction

The exchange between fluids and solids plays a key role in modeling and analysis of many natural phenomena. Therefore, fluid-structure interaction (FSI) is applied in numerous fields in industry and biomedical engineering, see e.g. [8, 25, 27]. An introduction into fluid-structure interaction can be found in classical monographs and textbooks, see [14, 29].

One of the main difficulties in the mathematical description of such problems lies in the choice of an appropriate coordinate system and dealing with the interface between the fluid and the structure. This results from the fluid equations being formulated in an Eulerian system, whereas the solid equations are defined in Lagrangian coordinates in their respective natural settings. As a direct consequence, modeling the information transfer on the interface between those different systems poses further challenges. Moreover, deformable objects can come into contact with each other resulting in changes to the topology of the computational domain and nonlinearities [6]. To this end, different frameworks have been developed, such as the Arbitrary Lagrangian Eulerian (ALE) method [10, 24], fictitious domain meth-

ods [19], immersed boundary methods [26], and fully Eulerian methods [11].

In this paper, we concentrate on an ALE approach and its application to the simulation of a falling elastic ball surrounded by a Newtonian fluid. We utilize a harmonic mesh motion PDE including a monitor function combined with a monolithic formulation, in which all occurring equations are solved simultaneously [5]. While this coupling introduces additional nonlinearities, the interface conditions, i.e. the continuity of the velocity and the normal stresses, are automatically fulfilled at each time step [13, 36].

The falling elastic ball is part of benchmark computations [35] and is also discussed in [12, 15]. It serves as an example for the combination of fluid-structure interaction and contact, which is subject of several research papers [2, 4, 31]. When the solid comes into contact with another solid or an exterior wall, like in the case of the falling ball, numerous numerical difficulties arise such as a change in the topology of the fluid domain and the Navier-Stokes no-collision paradox [22]. In our calculations, we will observe that a thin fluid layer always remains between the ball and the lower boundary due to the ALE approach, so any contact conditions are negligible. Furthermore, different extensions giving a physical meaning to this remaining fluid layer have been made [7, 16].

Von Wahl et al. [35] describes the application of different computational methods, such as ALE and fully Eulerian coordinates, to the falling ball and compares the results to experimental data. However, in that case contact and rebound of the ball are not realized in ALE. Frei et al. [15] focuses on the computational analysis of a fully Eulerian approach to the falling ball, whereas Fara et al. [12] employs an updated ALE method with re-meshing. In this paper, we provide a computational analysis of an alternative ALE approach, which utilizes a monitor function instead of re-meshing for improved mesh quality and is based on the work of Wick [37]. Therein, the goal is to achieve contact and rebound of the ball, thus proving the viability of the method in a large deformation scenario with contact. This setting is very challenging for ALE as the determinant of the deformation gradient tends to zero in the contact region. A good choice of the monitor function keeps a positive determinant allowing the ALE approach to continue to run.

The outline of this article is as follows. In Section 2, we describe the geometry of the falling elastic ball and formulate the PDE systems required to model the fluid as well as the solid. Moreover, we apply the transformations necessary to combine both systems in a monolithic approach. Next, we discretize and linearize the resulting system in Section 3. Having completed all the preliminary steps, we conduct numerical simulations in Section 4 and discuss our findings in two parameter studies. First, we set the physical parameters as in Frei et al. [15] and compare the results obtained with our ALE method to the fully Eulerian calculations. As a second example, we adjust the parameters in order to increase the dynamic of the system. Finally, in Section 5, we summarize our work and give concluding remarks.

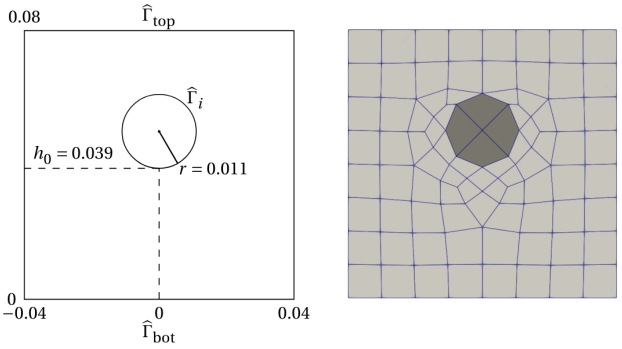

(a) Initial configuration of the falling elastic ball as in Frei et al. [15].

(b) Mesh for the initial configuration of the falling elastic ball with 1728 DoFs generated using Gmsh [17].

2 Geometry and PDE Systems

In this section, we cover the geometry of the falling elastic ball in its initial configuration and introduce the systems of partial differential equations for the fluid and the solid. Moreover, we derive the weak forms with the corresponding function spaces, transform the fluid equations into the reference configuration by means of the ALE mapping and combine the resulting equations in a monolithic approach. The PDE systems as well as the overall procedure are in alignment with the work by Wick [37].

2.1 Geometry

We consider a square-shaped domain with side length 0.08 m as in Frei et al. [15]. Inside the domain, the elastic ball with radius $r = 0.011$ m is positioned at the center with an initial height h_0 of 0.039 m. The remainder of the square is filled with an incompressible Newtonian fluid. This situation is illustrated in Figure 1a.

We assume the domain $\Omega(t) \subset \mathbb{R}^2$ to be time-dependent and split into two subdomains $\Omega_f(t)$ for the fluid and $\Omega_s(t)$ for the solid. The interface between the fluid and the solid is defined as:

$$\Gamma_i(t) := \partial\Omega_f(t) \cap \partial\Omega_s(t).$$

We also denote the upper exterior wall by $\Gamma_{\text{top}}(t)$, the lower exterior wall by $\Gamma_{\text{bot}}(t)$ and the entire outer boundary by $\Gamma(t)$. Moreover, we refer in the reference (i.e. the initial) configuration with $\widehat{\Omega}_\text{f}$ or $\widehat{\Omega}_\text{s}$ respectively to the subdomains and with $\widehat{\Gamma}_\text{i}$, $\widehat{\Gamma}_{\text{top}}$, $\widehat{\Gamma}_{\text{bot}}$ and $\widehat{\Gamma}$ to the initial interface and outer boundaries as highlighted in Figure 1a. For the time interval we define $t \in I = [0, T]$.

2.2 PDE Systems – Strong Form

We formulate the systems of partial differential equations for the fluid as well as the solid in strong form. We begin with the fluid by considering the incompressible, isothermal Navier-Stokes equations. Afterwards, we introduce the elasticity system for the solid.

Problem Statement 1 (Incompressible, Isothermal Navier-Stokes Equations)**.** Find a vector-valued velocity $\boldsymbol{v}_\text{f} : \Omega_\text{f}(t) \times I \to \mathbb{R}^2$ and a scalar-valued pressure $p_\text{f} : \Omega_\text{f}(t) \times I \to \mathbb{R}$ such that:

$$\begin{cases} \rho_\text{f}\partial_t \boldsymbol{v}_\text{f} + \rho_\text{f}(\boldsymbol{v}_\text{f}\cdot\nabla)\boldsymbol{v}_\text{f} - \nabla\cdot\boldsymbol{\sigma}_\text{f} = \rho_\text{f}\boldsymbol{f}_\text{f} & \text{in } \Omega_\text{f}(t)\times I, \\ \nabla\cdot\boldsymbol{v}_\text{f} = 0 & \text{in } \Omega_\text{f}(t)\times I, \\ \boldsymbol{v}_\text{f} = \boldsymbol{0} & \text{on } \left(\Gamma(t)\setminus\Gamma_{\text{top}}(t)\right)\times I, \\ (\boldsymbol{v}_\text{f})_y = 0 & \text{on } \Gamma_{\text{top}}(t)\times I, \\ (\boldsymbol{\sigma}_\text{f}\boldsymbol{n})_x = 0 & \text{on } \Gamma_{\text{top}}(t)\times I, \\ \boldsymbol{v}_\text{f} = \boldsymbol{v}_\text{f}^0 & \text{in } \Omega_\text{f}(0)\times\{0\}, \end{cases} \tag{1}$$

where ρ_f denotes the density of the fluid, $\boldsymbol{f}_\text{f}$ the external force acting on the fluid, $\boldsymbol{n}$ the outer normal vector, and $\boldsymbol{v}_\text{f}^0 : \Omega_\text{f}(0) \to \mathbb{R}^2$ initial values. The Cauchy stress tensor $\boldsymbol{\sigma}_\text{f}$ for a Newtonian incompressible fluid, i.e. the density of the fluid is characterized as constant in time through $\nabla\cdot\boldsymbol{v}_\text{f} = 0$, is defined as:

$$\boldsymbol{\sigma}_\text{f} := -p_\text{f}\boldsymbol{I} + \rho_\text{f}\nu_\text{f}(\nabla\boldsymbol{v}_\text{f} + \nabla\boldsymbol{v}_\text{f}^T)$$

with the identity matrix $\boldsymbol{I}$ and the kinematic viscosity ν_f of the fluid. In addition, we use the notation

$$\rho_\text{f}(\boldsymbol{v}_\text{f}\cdot\nabla)\boldsymbol{v}_\text{f} = \rho_\text{f}(\nabla\boldsymbol{v}_\text{f})\boldsymbol{v}_\text{f}.$$

Isothermal denotes the property that there is no change in temperature during the observed process.

The first boundary condition of Dirichlet type is referred to as the no-slip condition. The second boundary condition $(\boldsymbol{\sigma}_\text{f}\boldsymbol{n})_x = 0$ is a variation of the classical do-nothing outflow condition $\boldsymbol{\sigma}_\text{f}\boldsymbol{n} = \boldsymbol{0}$, which appears naturally on the variational level. While other conditions are also applicable, we make this choice since it includes a pressure normalization, see [21]. This is necessary due to only the gradient of the pressure p appearing in the Navier-Stokes equations. Hence, p is only defined up to a constant and with the normalization on the upper boundary we obtain pressure uniqueness. We note that the fluid equations are formulated in a time-dependent setting i.e. in Eulerian coordinates.

Problem Statement 2 (Elasticity System)**.** Find a vector-valued displacement $\widehat{\boldsymbol{u}}_\text{s} : \widehat{\Omega}_\text{s}\times I \to \mathbb{R}^2$ such that:

$$\begin{cases} \widehat{\rho}_\text{s}\partial_t^2\widehat{\boldsymbol{u}}_\text{s} - \widehat{\nabla}\cdot(\widehat{\boldsymbol{F}}\widehat{\boldsymbol{\Sigma}}_\text{s}) = \widehat{\rho}_\text{s}\widehat{\boldsymbol{f}}_\text{s} & \text{in } \widehat{\Omega}_\text{s}\times I, \\ \widehat{\boldsymbol{u}}_\text{s} = \widehat{\boldsymbol{u}}_\text{s}^0 & \text{in } \widehat{\Omega}_\text{s}\times\{0\}, \end{cases}$$

where $\widehat{\rho}_\text{s}$ denotes the density of the solid, $\widehat{\boldsymbol{f}}_\text{s}$ the external force acting on the solid, $\widehat{\boldsymbol{u}}_\text{s}^0 : \widehat{\Omega}_\text{s} \to \mathbb{R}^2$ initial values and $\widehat{\boldsymbol{F}} := \boldsymbol{I} + \widehat{\nabla}\widehat{\boldsymbol{u}}$ the deformation gradient. $\widehat{\boldsymbol{\Sigma}}_\text{s}$ is the second Piola-Kirchhoff tensor for Saint Venant-Kirchhoff (STVK) materials. It is defined as:

$$\widehat{\boldsymbol{\Sigma}}_\text{s} := \lambda_\text{s}(\text{tr}\widehat{\boldsymbol{E}})\boldsymbol{I} + 2\mu_\text{s}\widehat{\boldsymbol{E}}.$$

Therein $\widehat{\boldsymbol{E}} := \frac{1}{2}(\widehat{\boldsymbol{F}}^T\widehat{\boldsymbol{F}} - \boldsymbol{I})$ connotes the Green-Lagrange strain tensor and λ_s, μ_s the Lamé parameters.

STVK materials are characterized as isotropic and homogeneous. However, STVK is suitable for small strains only. Note that, in contrast to the fluid equations, the elasticity system for the solid is formulated in the reference configuration, i.e. in Lagrangian coordinates. Furthermore, we notice that the solid equations can be reduced to a first order in time system by introducing the velocity $\widehat{\boldsymbol{v}}_\text{s}$.

Problem Statement 3 (Elasticity System – Mixed Formulation)**.** Find a vector-valued displacement $\widehat{\boldsymbol{u}}_\text{s} : \widehat{\Omega}_\text{s}\times I \to \mathbb{R}^2$ and a vector-valued velocity $\widehat{\boldsymbol{v}}_\text{s} : \widehat{\Omega}_\text{s}\times I \to \mathbb{R}^2$ such that:

$$\begin{cases} \widehat{\rho}_\text{s}\partial_t\widehat{\boldsymbol{v}}_\text{s} - \widehat{\nabla}\cdot(\widehat{\boldsymbol{F}}\widehat{\boldsymbol{\Sigma}}_\text{s}) = \widehat{\rho}_\text{s}\widehat{\boldsymbol{f}}_\text{s} & \text{in } \widehat{\Omega}_\text{s}\times I, \\ \partial_t\widehat{\boldsymbol{u}}_\text{s} - \widehat{\boldsymbol{v}}_\text{s} = \boldsymbol{0} & \text{in } \widehat{\Omega}_\text{s}\times I, \\ \widehat{\boldsymbol{u}}_\text{s} = \widehat{\boldsymbol{u}}_\text{s}^0 & \text{in } \widehat{\Omega}_\text{s}\times\{0\}, \\ \widehat{\boldsymbol{v}}_\text{s} = \widehat{\boldsymbol{v}}_\text{s}^0 & \text{in } \widehat{\Omega}_\text{s}\times\{0\}, \end{cases} \tag{2}$$

with initial values $\widehat{\boldsymbol{v}}_\text{s}^0 : \widehat{\Omega}_\text{s} \to \mathbb{R}^2$ and all previous definitions.

In the statement above we prescribe no boundary conditions for the solid equations since the only boundary of $\widehat{\Omega}_\text{s}$ is the interface between the fluid and the solid domain, see Figure 1a. However, we require two coupling conditions on the interface, which can be stated in the reference configuration as follows:

$$\begin{cases} \widehat{\boldsymbol{v}}_\text{f} = \widehat{\boldsymbol{v}}_\text{s} & \text{on } \widehat{\Gamma}_\text{i}, \\ \widehat{\boldsymbol{F}}\widehat{\boldsymbol{\Sigma}}_\text{s}\widehat{\boldsymbol{n}}_\text{s} + \widehat{J}\boldsymbol{\sigma}_\text{f}\widehat{\boldsymbol{F}}^{-T}\widehat{\boldsymbol{n}}_\text{f} = \boldsymbol{0} & \text{on } \widehat{\Gamma}_\text{i}, \end{cases} \tag{3}$$

where $\widehat{J} = \det(\widehat{\boldsymbol{F}})$ and $\widehat{\boldsymbol{n}}_\text{s}, \widehat{\boldsymbol{n}}_\text{f}$ denote the outer normal vector as seen from $\widehat{\Omega}_\text{s}$ and $\widehat{\Omega}_\text{f}$ respectively.

The first condition of Dirichlet type is referred to as the kinematic condition and the second of Neumann type is called dynamic condition. We will see that these conditions are automatically fulfilled on a variational level with our monolithic approach.

2.3 Function Spaces

In order to derive the weak forms of our previously stated systems, we first define the function spaces for all considered quantities, as done in classical PDE literature, e.g., [39].

We denote a scalar product on a Hilbert space X as $(\cdot,\cdot)_X$ and use the notation $\langle\cdot,\cdot\rangle_{\partial X}$ for the scalar product on the boundary. By $L^p(\Omega)$, $1 \le p \le \infty$, we refer to the standard Lebesgue spaces, which consist of measurable functions f that are Lebesgue-integrable to the p-th power. By considering the norm $\|\cdot\|_{L^p}$, $\left(L^p(\Omega), \|\cdot\|_{L^p}\right)$ forms a Banach space and for $p=2$, the Sobolev spaces $H^m(\Omega) := W^{m,2}(\Omega)$ are Hilbert spaces with norm $\|\cdot\|_{H^m}$. For functions $u \in H^m(\Omega)$ with zero trace on some part of the boundary $\Gamma_{\mathrm{D}} \subset \partial\Omega$ we define

$$H^m_{\Gamma_{\mathrm{D}}}(\Omega) := \left\{ u \in H^m(\Omega) : u|_{\Gamma_{\mathrm{D}}} = 0 \right\}.$$

2.4 PDE Systems – Weak Forms and ALE-Transformation

The derivation of the weak forms follows the usual procedure: 1) Define the function spaces for all solution variables. 2) Multiply with a test function, integrate over the domain and employ integration by parts.

We showcase this process by example of the Navier-Stokes equations and begin by defining the function spaces for the vector-valued velocity $\boldsymbol{v}_{\mathrm{f}}$ and the scalar valued pressure p_{f} for a fixed $t \in I$ using the spaces from Section 2.3:

$$\boldsymbol{v}_{\mathrm{f}} = \left((\boldsymbol{v}_{\mathrm{f}})_x, (\boldsymbol{v}_{\mathrm{f}})_y \right) \in H^1_{\Gamma\setminus\Gamma_{\mathrm{top}}}(\Omega_{\mathrm{f}}) \times H^1_{\Gamma}(\Omega_{\mathrm{f}}),$$
$$p_{\mathrm{f}} \in L^2(\Omega_{\mathrm{f}}).$$

We here omitted the time variable t for simplicity. Nevertheless, we still consider the fluid domain Ω_{f} to be time-dependent. As usual, we include all Dirichlet boundary conditions into the function space and choose the regularity of the solution functions with respect to the required derivative information. We now multiply the Navier-Stokes equations (1) with a test function and integrate over the fluid domain Ω_{f}:

Let $t \in I$, $\boldsymbol{\Phi}^v = \left((\boldsymbol{\Phi}^v)_x, (\boldsymbol{\Phi}^v)_y \right) \in H^1_{\Gamma\setminus\Gamma_{\mathrm{top}}}(\Omega_{\mathrm{f}}) \times H^1_{\Gamma}(\Omega_{\mathrm{f}})$, $\Phi^p \in L^2(\Omega_{\mathrm{f}})$ be arbitrary. It holds:

$$\int_{\Omega_{\mathrm{f}}} \rho_{\mathrm{f}} \partial_t \boldsymbol{v}_{\mathrm{f}} \boldsymbol{\Phi}^v \, dx + \int_{\Omega_{\mathrm{f}}} \rho_{\mathrm{f}} (\boldsymbol{v}_{\mathrm{f}} \cdot \nabla) \boldsymbol{v}_{\mathrm{f}} \boldsymbol{\Phi}^v \, dx - \int_{\Omega_{\mathrm{f}}} \nabla \cdot \boldsymbol{\sigma}_{\mathrm{f}} \boldsymbol{\Phi}^v \, dx = \int_{\Omega_{\mathrm{f}}} \rho_{\mathrm{f}} \boldsymbol{f}_{\mathrm{f}} \boldsymbol{\Phi}^v \, dx,$$
$$\int_{\Omega_{\mathrm{f}}} \nabla \cdot \boldsymbol{v}_{\mathrm{f}} \Phi^p \, dx = 0.$$

We remark that in the above equation and in the following we omit for simplicity the dot denoting the scalar product between two vectors, i.e. terms like $\partial_t \boldsymbol{v}_{\mathrm{f}} \boldsymbol{\Phi}^v$ are to be interpreted as $\partial_t \boldsymbol{v}_{\mathrm{f}} \cdot \boldsymbol{\Phi}^v$.

The next step is to apply integration by parts to the third term:

$$\int_{\Omega_{\mathrm{f}}} \nabla \cdot \boldsymbol{\sigma}_{\mathrm{f}} \boldsymbol{\Phi}^v \, dx = \int_{\Gamma} \boldsymbol{\sigma}_{\mathrm{f}} \boldsymbol{n} \boldsymbol{\Phi}^v \, ds + \int_{\Gamma_{\mathrm{i}}} \boldsymbol{\sigma}_{\mathrm{f}} \boldsymbol{n}_{\mathrm{f}} \boldsymbol{\Phi}^v \, ds - \int_{\Omega_{\mathrm{f}}} \boldsymbol{\sigma}_{\mathrm{f}} : \nabla \boldsymbol{\Phi}^v \, dx.$$

Here $\boldsymbol{\sigma}_{\mathrm{f}} : \nabla \boldsymbol{\Phi}^v$ denotes the Frobenius inner product. We notice that on all parts of the outer boundary and for both components it holds either $\boldsymbol{\Phi}^v = \boldsymbol{0}$ or $\boldsymbol{\sigma}_{\mathrm{f}} \boldsymbol{n} = \boldsymbol{0}$. Hence, the integral over the outer boundary vanishes. With these calculations, we can now formulate the Navier-Stokes equations in weak form.

Problem Statement 4 (Navier-Stokes Equations – Weak Form)**.** For almost all (in a Lebesgue sense) $t \in I$, find $\boldsymbol{v}_{\mathrm{f}} \in H^1_{\Gamma\setminus\Gamma_{\mathrm{top}}}(\Omega_{\mathrm{f}}) \times H^1_{\Gamma}(\Omega_{\mathrm{f}})$ and $p_{\mathrm{f}} \in L^2(\Omega_{\mathrm{f}})$ satisfying $\boldsymbol{v}_{\mathrm{f}}(0) = \boldsymbol{v}_{\mathrm{f}}^0$ such that:

$$\begin{aligned} \int_{\Omega_{\mathrm{f}}} \rho_{\mathrm{f}} \partial_t \boldsymbol{v}_{\mathrm{f}} \boldsymbol{\Phi}^v \, dx + \int_{\Omega_{\mathrm{f}}} \rho_{\mathrm{f}} (\boldsymbol{v}_{\mathrm{f}} \cdot \nabla) \boldsymbol{v}_{\mathrm{f}} \boldsymbol{\Phi}^v \, dx + \int_{\Omega_{\mathrm{f}}} \boldsymbol{\sigma}_{\mathrm{f}} : \nabla \boldsymbol{\Phi}^v \, dx \\ - \int_{\Gamma_{\mathrm{i}}} \boldsymbol{\sigma}_{\mathrm{f}} \boldsymbol{n}_{\mathrm{f}} \boldsymbol{\Phi}^v \, ds = \int_{\Omega_{\mathrm{f}}} \rho_{\mathrm{f}} \boldsymbol{f}_{\mathrm{f}} \boldsymbol{\Phi}^v \, dx, \\ \int_{\Omega_{\mathrm{f}}} \nabla \cdot \boldsymbol{v}_{\mathrm{f}} \Phi^p \, dx = 0, \end{aligned} \tag{4}$$

for all $\boldsymbol{\Phi}^v \in H^1_{\Gamma\setminus\Gamma_{\mathrm{top}}}(\Omega_{\mathrm{f}}) \times H^1_{\Gamma}(\Omega_{\mathrm{f}})$, $\Phi^p \in L^2(\Omega_{\mathrm{f}})$.

By the same means we can derive the weak form for the equations of the elasticity system (2).

Problem Statement 5 (Elasticity System – Weak Form)**.** For almost all $t \in I$, find $\widehat{\boldsymbol{u}}_{\mathrm{s}} \in \left(H^1(\widehat{\Omega}_{\mathrm{s}}) \right)^2$ and $\widehat{\boldsymbol{v}}_{\mathrm{s}} \in \left(L^2(\widehat{\Omega}_{\mathrm{s}}) \right)^2$ satisfying $\widehat{\boldsymbol{u}}_{\mathrm{s}}(0) = \widehat{\boldsymbol{u}}_{\mathrm{s}}^0$ and $\widehat{\boldsymbol{v}}_{\mathrm{s}}(0) = \widehat{\boldsymbol{v}}_{\mathrm{s}}^0$ such that:

$$\begin{aligned} \int_{\widehat{\Omega}_{\mathrm{s}}} \widehat{\rho}_{\mathrm{s}} \partial_t \widehat{\boldsymbol{v}}_{\mathrm{s}} \widehat{\boldsymbol{\Phi}}^u \, d\widehat{x} + \int_{\widehat{\Omega}_{\mathrm{s}}} \widehat{\boldsymbol{F}} \widehat{\boldsymbol{\Sigma}}_{\mathrm{s}} : \widehat{\nabla} \widehat{\boldsymbol{\Phi}}^u \, d\widehat{x} - \int_{\widehat{\Gamma}_{\mathrm{i}}} \widehat{\boldsymbol{F}} \widehat{\boldsymbol{\Sigma}}_{\mathrm{s}} \widehat{\boldsymbol{n}}_{\mathrm{s}} \widehat{\boldsymbol{\Phi}}^u \, d\widehat{s} = \int_{\widehat{\Omega}_{\mathrm{s}}} \widehat{\rho}_{\mathrm{s}} \widehat{\boldsymbol{f}}_{\mathrm{s}} \widehat{\boldsymbol{\Phi}}^u \, d\widehat{x}, \\ \int_{\widehat{\Omega}_{\mathrm{s}}} (\partial_t \widehat{\boldsymbol{u}}_{\mathrm{s}} - \widehat{\boldsymbol{v}}_{\mathrm{s}}) \widehat{\boldsymbol{\Phi}}^v \, d\widehat{x} = 0, \end{aligned} \tag{5}$$

for all $\widehat{\boldsymbol{\Phi}}^u \in \left(H^1(\widehat{\Omega}_{\mathrm{s}}) \right)^2$, $\widehat{\boldsymbol{\Phi}}^v \in \left(L^2(\widehat{\Omega}_{\mathrm{s}}) \right)^2$.

We couple these variational formulations via a monolithic approach in the ALE framework. Therefore, we introduce the vector-valued fluid mesh displacement $\widehat{\boldsymbol{u}}_{\mathrm{f}}$ and the ALE mapping $\widehat{\mathscr{A}}$ in order to transform the fluid equations into the reference configuration, a procedure first introduced by Hron and Turek in [23].

The construction of $\widehat{\boldsymbol{u}}_{\mathrm{f}}$ is driven by the motion of the interface and thus fulfills $\widehat{\boldsymbol{u}}_{\mathrm{f}} = \widehat{\boldsymbol{u}}_{\mathrm{s}}$ on $\widehat{\Gamma}_{\mathrm{i}}$. Note that this implies the following kinematic coupling condition on $\widehat{\Gamma}_{\mathrm{i}}$:

$$\widehat{\boldsymbol{v}}_{\mathrm{f}} = \partial_t \widehat{\boldsymbol{u}}_{\mathrm{f}} = \partial_t \widehat{\boldsymbol{u}}_{\mathrm{s}} = \widehat{\boldsymbol{v}}_{\mathrm{s}}.$$

Moreover, we restrict any motion of the exterior walls by setting $\widehat{\boldsymbol{u}}_\mathrm{f} = \mathbf{0}$ on the entire outer boundary $\widehat{\Gamma}$ apart from the upper and lower exterior wall. There we prescribe Neumann boundary conditions for the x-component of $\widehat{\boldsymbol{u}}_\mathrm{f}$ instead. The movement of the interface is then extended into the entire fluid domain by means of an auxiliary problem, a so-called mesh motion PDE (MMPDE). In our case we consider a harmonic model which reads as follows:

$$\begin{cases} -\widehat{\nabla}\cdot\widehat{\boldsymbol{\sigma}}_\mathrm{mesh} = 0 & \text{in } \widehat{\Omega}_\mathrm{f}\times I, \\ \widehat{\boldsymbol{u}}_\mathrm{f} = \widehat{\boldsymbol{u}}_\mathrm{s} & \text{on } \widehat{\Gamma}_\mathrm{i}\times I, \\ \widehat{\boldsymbol{u}}_\mathrm{f} = \mathbf{0} & \text{on } \widehat{\Gamma}\setminus(\widehat{\Gamma}_\mathrm{top}\cup\widehat{\Gamma}_\mathrm{bot})\times I, \\ (\widehat{\boldsymbol{u}}_\mathrm{f})_y = 0 & \text{on } \widehat{\Gamma}_\mathrm{top}\cup\widehat{\Gamma}_\mathrm{bot}\times I, \\ \widehat{\nabla}(\widehat{\boldsymbol{u}}_\mathrm{f})_x\widehat{\boldsymbol{n}} = 0 & \text{on } \widehat{\Gamma}_\mathrm{top}\cup\widehat{\Gamma}_\mathrm{bot}\times I, \end{cases} \tag{6}$$

where $\widehat{\boldsymbol{\sigma}}_\mathrm{mesh} := \alpha_u\widehat{\nabla}\widehat{\boldsymbol{u}}_\mathrm{f}$ with a monitor function $\alpha_u := \alpha_u(\widehat{\boldsymbol{x}})$ that we will specify later on. The weak form of the MMPDE can be derived by the same procedure we have already seen for the Navier-Stokes equations in (4). As a result of the chosen boundary conditions, only the boundary integral on the interface remains.

Next, we introduce the ALE mapping $\widehat{\mathscr{A}}$.

Definition 6 (ALE mapping)**.** The ALE mapping is defined as follows:

$$\widehat{\mathscr{A}} : \widehat{\Omega}_\mathrm{f}\times I \to \Omega_\mathrm{f}(t), \quad \widehat{\mathscr{A}}(\widehat{\boldsymbol{x}},t) = \widehat{\boldsymbol{x}} + \widehat{\boldsymbol{u}}_\mathrm{f}(\widehat{\boldsymbol{x}},t). \tag{7}$$

We assume $\widehat{\mathscr{A}}$ to be a C^1-diffeomorphism, i.e. sufficiently regular to apply change of variables. Furthermore, we define:

$$\widehat{\boldsymbol{F}} := \widehat{\nabla}\widehat{\mathscr{A}} = \boldsymbol{I} + \widehat{\nabla}\widehat{\boldsymbol{u}}_\mathrm{f}, \quad \widehat{J} := \det(\widehat{\boldsymbol{F}}),$$

where the definition of the deformation gradient $\widehat{\boldsymbol{F}}$ in $\widehat{\Omega}_\mathrm{f}$ corresponds to the notation in $\widehat{\Omega}_\mathrm{s}$, see equation (2). For a function $\widehat{\boldsymbol{f}} \in C^1(\widehat{\Omega}_\mathrm{f}\times I, \mathbb{R}^2)$ we denote the ALE time derivative by

$$\widehat{\partial}_t\widehat{\boldsymbol{f}} := \frac{d}{dt}\widehat{\boldsymbol{f}}.$$

Using this mapping in combination with change of variables, we can now transform the fluid equations into the reference configuration. To this end, we first provide some transformation rules which are proven in [29, Lemma 2.3]. We repeat the theorem here for convenience of the reader.

Theorem 7 (Transformation rules)**.** *Let $\boldsymbol{f} \in C^1(\Omega_\mathrm{f}(t)\times I, \mathbb{R}^2)$ be a function in Eulerian coordinates, $\widehat{\mathscr{A}}$ the ALE mapping and $\widehat{\boldsymbol{f}}(\widehat{\boldsymbol{x}},t) = \boldsymbol{f}(\widehat{\mathscr{A}}(\widehat{\boldsymbol{x}},t),t) \in C^1(\widehat{\Omega}_\mathrm{f}\times I, \mathbb{R}^2)$ the function in Lagrangian coordinates corresponding to $\boldsymbol{f}$. It holds:*

i) $\nabla\widehat{\boldsymbol{f}} = \widehat{\nabla}\widehat{\boldsymbol{f}}\widehat{\boldsymbol{F}}^{-1}$,

ii) $\widehat{\partial}_t\widehat{\boldsymbol{f}} = \partial_t\widehat{\boldsymbol{f}} + \widehat{\boldsymbol{F}}^{-1}(\partial_t\widehat{\boldsymbol{u}}_\mathrm{f}\cdot\widehat{\nabla})\widehat{\boldsymbol{f}}$.

We consider the Navier-Stokes equations in weak form (4) term by term and apply change of variables with the previously shown transformation rules:

$$\int_{\Omega_\mathrm{f}} \rho_\mathrm{f}\partial_t\boldsymbol{v}_\mathrm{f}\boldsymbol{\Phi}^v\,dx = \int_{\widehat{\Omega}_\mathrm{f}} \widehat{\rho}_\mathrm{f}\widehat{J}\left(\widehat{\partial}_t\widehat{\boldsymbol{v}}_\mathrm{f} - (\widehat{\boldsymbol{F}}^{-1}\partial_t\widehat{\boldsymbol{u}}_\mathrm{f}\cdot\widehat{\nabla})\widehat{\boldsymbol{v}}_\mathrm{f}\right)\widehat{\boldsymbol{\Phi}}^v\,d\widehat{x}$$

where we utilized transformation rule ii).

$$\int_{\Omega_\mathrm{f}} \rho_\mathrm{f}(\boldsymbol{v}_\mathrm{f}\cdot\nabla)\boldsymbol{v}_\mathrm{f}\boldsymbol{\Phi}^v\,dx = \int_{\widehat{\Omega}_\mathrm{f}} \widehat{\rho}_\mathrm{f}\widehat{J}(\widehat{\boldsymbol{F}}^{-1}\widehat{\boldsymbol{v}}_\mathrm{f}\cdot\widehat{\nabla})\widehat{\boldsymbol{v}}_\mathrm{f}\widehat{\boldsymbol{\Phi}}^v\,d\widehat{x},$$

which includes transformation rule i).

$$\int_{\Omega_\mathrm{f}} \boldsymbol{\sigma}_\mathrm{f} : \nabla\boldsymbol{\Phi}^v\,dx = \int_{\widehat{\Omega}_\mathrm{f}} \widehat{J}\boldsymbol{\sigma}_\mathrm{f}\widehat{\boldsymbol{F}}^{-T} : \widehat{\nabla}\widehat{\boldsymbol{\Phi}}^v\,d\widehat{x},$$

where we applied the Piola transformation that reads $\widehat{\boldsymbol{\sigma}}_\mathrm{f} = \widehat{J}\boldsymbol{\sigma}_\mathrm{f}\widehat{\boldsymbol{F}}^{-T}$.

$$\int_{\Gamma_\mathrm{i}} \boldsymbol{\sigma}_\mathrm{f}\boldsymbol{n}_\mathrm{f}\boldsymbol{\Phi}^v\,ds = \int_{\widehat{\Gamma}_\mathrm{i}} \widehat{J}\boldsymbol{\sigma}_\mathrm{f}\widehat{\boldsymbol{F}}^{-T}\widehat{\boldsymbol{n}}_\mathrm{f}\widehat{\boldsymbol{\Phi}}^v\,d\widehat{s},$$

in which we used Nansons's formula: $\boldsymbol{n}\,ds = \widehat{J}\widehat{\boldsymbol{F}}^{-T}\widehat{\boldsymbol{n}}\,d\widehat{s}$. The right hand side of the first equation is transformed directly by change of variables without the need for further rules, which is why we omit it here. Finally, we turn to the incompressibility condition:

$$\int_{\Omega_\mathrm{f}} \nabla\cdot\boldsymbol{v}_\mathrm{f}\Phi^p\,dx = \int_{\widehat{\Omega}_\mathrm{f}} \widehat{J}\widehat{\nabla}\cdot(\widehat{\boldsymbol{F}}^{-1}\widehat{\boldsymbol{v}}_\mathrm{f})\widehat{\Phi}^p\,d\widehat{x},$$

where we utilized $\nabla\cdot\boldsymbol{v}_\mathrm{f} = \mathrm{tr}(\nabla\boldsymbol{v}_\mathrm{f})$, transformation rule i) and that the trace is invariant under cyclic permutations.

With these computations, we can now state the transformed Navier-Stokes equations in the reference configuration.

Problem Statement 8 (Transformed Navier-Stokes Equations)**.** For almost all $t \in I$, find $\widehat{\boldsymbol{v}}_\mathrm{f} \in H^1_{\widehat{\Gamma}\setminus\widehat{\Gamma}_\mathrm{top}}(\widehat{\Omega}_\mathrm{f}) \times H^1_{\widehat{\Gamma}}(\widehat{\Omega}_\mathrm{f})$ and $\widehat{p}_\mathrm{f} \in L^2(\widehat{\Omega}_\mathrm{f})$ satisfying $\widehat{\boldsymbol{v}}_\mathrm{f}(0) = \widehat{\boldsymbol{v}}_\mathrm{f}^0$ such that:

$$\begin{aligned} &\int_{\widehat{\Omega}_\mathrm{f}} \widehat{\rho}_\mathrm{f}\widehat{J}\widehat{\partial}_t\widehat{\boldsymbol{v}}_\mathrm{f}\widehat{\boldsymbol{\Phi}}^v\,d\widehat{x} + \int_{\widehat{\Omega}_\mathrm{f}} \widehat{\rho}_\mathrm{f}\widehat{J}\left(\widehat{\boldsymbol{F}}^{-1}(\widehat{\boldsymbol{v}}_\mathrm{f} - \partial_t\widehat{\boldsymbol{u}}_\mathrm{f})\cdot\widehat{\nabla}\right)\widehat{\boldsymbol{v}}_\mathrm{f}\widehat{\boldsymbol{\Phi}}^v\,d\widehat{x} \\ &+ \int_{\widehat{\Omega}_\mathrm{f}} \widehat{J}\boldsymbol{\sigma}_\mathrm{f}\widehat{\boldsymbol{F}}^{-T} : \widehat{\nabla}\widehat{\boldsymbol{\Phi}}^v\,d\widehat{x} - \int_{\widehat{\Gamma}_\mathrm{i}} \widehat{J}\boldsymbol{\sigma}_\mathrm{f}\widehat{\boldsymbol{F}}^{-T}\widehat{\boldsymbol{n}}_\mathrm{f}\widehat{\boldsymbol{\Phi}}^v\,d\widehat{s} = \int_{\widehat{\Omega}_\mathrm{f}} \widehat{\rho}_\mathrm{f}\widehat{J}\widehat{\boldsymbol{f}}_\mathrm{f}\widehat{\boldsymbol{\Phi}}^v\,d\widehat{x}, \\ &\int_{\widehat{\Omega}_\mathrm{f}} \widehat{J}\widehat{\nabla}\cdot(\widehat{\boldsymbol{F}}^{-1}\widehat{\boldsymbol{v}}_\mathrm{f})\widehat{\Phi}^p\,d\widehat{x} = 0, \end{aligned} \tag{8}$$

for all $\widehat{\boldsymbol{\Phi}}^v \in H^1_{\widehat{\Gamma}\setminus\widehat{\Gamma}_\mathrm{top}}(\widehat{\Omega}_\mathrm{f}) \times H^1_{\widehat{\Gamma}}(\widehat{\Omega}_\mathrm{f})$, $\widehat{\Phi}^p \in L^2(\widehat{\Omega}_\mathrm{f})$.

At this point, the elasticity system in weak form (5), the transformed Navier-Stokes equations (8) and the MMPDE (6) are defined in the same coordinates. Hence, we can couple them with a monolithic approach. This is justified due to the kinematic condition and the definition of $\widehat{\boldsymbol{u}}_\mathrm{f}$:

$$\widehat{\boldsymbol{v}}_\mathrm{f} = \widehat{\boldsymbol{v}}_\mathrm{s} \text{ on } \widehat{\Gamma}_\mathrm{i} \text{ and } \widehat{\boldsymbol{u}}_\mathrm{f} = \widehat{\boldsymbol{u}}_\mathrm{s} \text{ on } \widehat{\Gamma}_\mathrm{i}.$$

We also extend the pressure discontinuously into the whole domain by setting it to zero in $\widehat{\Omega}_\mathrm{s}$.

Moreover, we are now able to define the control parameter $\alpha_u(\widehat{\boldsymbol{x}}) := \alpha\widehat{J}^{-1}$, where α is a constant factor. This strategy was proposed by Tezduyar et al. [32] and further developed by Stein et al. [30]. Furthermore, it was intensively utilized in [38] for a computational analysis of the Turek-Hron FSI benchmarks [34]. As $\widehat{J}$ is the determinant of the deformation gradient, it is directly related to the mesh deformation and in particular assumes small values for large deformations. By choosing the control parameter α_u as the inverse of $\widehat{J}$, we therefore put stronger emphasis on the mesh motion PDE in large deformation cases guaranteeing satisfactory fluid mesh quality.

This allows us to formulate our final variational monolithic ALE-FSI problem by additively combining the first equation of the Navier-Stokes equations and the first equation of the elasticity system into one expression. The same procedure is applied to the MMPDE and the second equation of the elasticity system. In the following we abbreviate the integrals with the L^2 scalar product and the notation introduced in Section 2.3. Additionally, we simplify the definition of the function spaces:

$$\widehat{\mathcal{V}}^0 := H^1_{\widehat{\Gamma}\setminus\widehat{\Gamma}_\mathrm{top}}(\widehat{\Omega}) \times H^1_{\widehat{\Gamma}}(\widehat{\Omega}),\ \widehat{\mathcal{V}}^1 := H^1_{\widehat{\Gamma}\setminus(\widehat{\Gamma}_\mathrm{top}\cup\widehat{\Gamma}_\mathrm{bot})}(\widehat{\Omega}) \times H^1_{\widehat{\Gamma}}(\widehat{\Omega}).$$

Problem Statement 9 (Variational Monolithic ALE-FSI Problem)**.** For almost all $t \in I$, find $\widehat{\boldsymbol{v}} \in \widehat{\mathcal{V}}^0$, $\widehat{\boldsymbol{u}} \in \widehat{\mathcal{V}}^1$ and $\widehat{p} \in L^2(\widehat{\Omega})$ satisfying $\widehat{\boldsymbol{v}}(0) = \widehat{\boldsymbol{v}}^0$ and $\widehat{\boldsymbol{u}}(0) = \widehat{\boldsymbol{u}}^0$ such that:

$$\begin{aligned}
&(\widehat{\rho}_\mathrm{f}\widehat{J}\widehat{\partial}_t\widehat{\boldsymbol{v}}, \widehat{\boldsymbol{\Phi}}^v)_{\widehat{\Omega}_\mathrm{f}} + (\widehat{\rho}_\mathrm{f}\widehat{J}(\widehat{\boldsymbol{F}}^{-1}(\widehat{\boldsymbol{v}} - \partial_t\widehat{\boldsymbol{u}})\cdot\widehat{\nabla})\widehat{\boldsymbol{v}}, \widehat{\boldsymbol{\Phi}}^v)_{\widehat{\Omega}_\mathrm{f}} \\
&\qquad + (\widehat{J}\boldsymbol{\sigma}_\mathrm{f}\widehat{\boldsymbol{F}}^{-T}, \widehat{\nabla}\widehat{\boldsymbol{\Phi}}^v)_{\widehat{\Omega}_\mathrm{f}} + (\widehat{\rho}_\mathrm{s}\partial_t\widehat{\boldsymbol{v}}, \widehat{\boldsymbol{\Phi}}^v)_{\widehat{\Omega}_\mathrm{s}} \\
&\qquad + (\widehat{\boldsymbol{F}}\widehat{\boldsymbol{\Sigma}}_\mathrm{s}, \widehat{\nabla}\widehat{\boldsymbol{\Phi}}^v)_{\widehat{\Omega}_\mathrm{s}} \\
&\qquad = (\widehat{\rho}_\mathrm{f}\widehat{J}\widehat{\boldsymbol{f}}_\mathrm{f}, \widehat{\boldsymbol{\Phi}}^v)_{\widehat{\Omega}_\mathrm{f}} + (\widehat{\rho}_\mathrm{s}\widehat{\boldsymbol{f}}_\mathrm{s}, \widehat{\boldsymbol{\Phi}}^v)_{\widehat{\Omega}_\mathrm{s}}, \\
&(\partial_t\widehat{\boldsymbol{u}} - \widehat{\boldsymbol{v}}, \widehat{\boldsymbol{\Phi}}^u)_{\widehat{\Omega}_\mathrm{s}} + (\alpha\widehat{J}^{-1}\widehat{\nabla}\widehat{\boldsymbol{u}}, \widehat{\nabla}\widehat{\boldsymbol{\Phi}}^u)_{\widehat{\Omega}_\mathrm{f}} - \langle\alpha\widehat{J}^{-1}\widehat{\nabla}\widehat{\boldsymbol{u}}_\mathrm{f}\widehat{\boldsymbol{n}}_\mathrm{f}, \widehat{\boldsymbol{\Phi}}^u\rangle_{\widehat{\Gamma}_\mathrm{i}} = 0, \\
&(\widehat{J}\widehat{\nabla}\cdot(\widehat{\boldsymbol{F}}^{-1}\widehat{\boldsymbol{v}}_\mathrm{f}), \widehat{\Phi}^p)_{\widehat{\Omega}_\mathrm{f}} = 0,
\end{aligned} \tag{9}$$

for all $\widehat{\boldsymbol{\Phi}}^v \in \widehat{\mathcal{V}}^0$, $\widehat{\boldsymbol{\Phi}}^u \in \widehat{\mathcal{V}}^1$, $\widehat{\Phi}^p \in L^2(\widehat{\Omega})$. In short we also denote this system by

$$\widehat{\boldsymbol{A}}(\widehat{\boldsymbol{v}}, \widehat{\boldsymbol{u}}, \widehat{p})(\widehat{\boldsymbol{\Phi}}) = \widehat{\boldsymbol{F}}(\widehat{\boldsymbol{\Phi}}). \tag{10}$$

Here $\widehat{\boldsymbol{\Phi}} = (\widehat{\boldsymbol{\Phi}}^v, \widehat{\boldsymbol{\Phi}}^u, \widehat{\Phi}^p)$ denotes the test functions, all left hand side terms are collected in the semi-linear form $\widehat{\boldsymbol{A}}$ (i.e. $\widehat{\boldsymbol{A}}$ is non-linear in $(\widehat{\boldsymbol{v}}, \widehat{\boldsymbol{u}}, \widehat{p})$ but linear in $\widehat{\boldsymbol{\Phi}}$) and all right hand side terms are summarized in $\widehat{\boldsymbol{F}}$.

Note that the interface integrals cancel out with the dynamic coupling condition, see equation (3):

$$\int_{\widehat{\Gamma}_\mathrm{i}} \widehat{\boldsymbol{F}}\widehat{\boldsymbol{\Sigma}}_\mathrm{s}\widehat{\boldsymbol{n}}_\mathrm{s}\widehat{\boldsymbol{\Phi}}^v\, d\widehat{s} + \int_{\widehat{\Gamma}_\mathrm{i}} \widehat{J}\boldsymbol{\sigma}_\mathrm{f}\widehat{\boldsymbol{F}}^{-T}\widehat{\boldsymbol{n}}_\mathrm{f}\widehat{\boldsymbol{\Phi}}^v\, d\widehat{s} = 0.$$

Together with the continuous extension of $\widehat{\boldsymbol{v}}$, this ensures that both the kinematic and the dynamic coupling condition are already fulfilled. Hence, no adjustments in the solution algorithm are required to account for them.

Having stated our final equation system, we now turn to its discretization and linearization.

3 Discretization and Linearization

For the discretization and linearization we proceed as in Wick [37]. We first apply the Rothe method to discretize in time and space. This results in a non-linear equation system, which we will linearize by means of a line search Newton method.

3.1 Discretization – Rothe method

The Rothe method consists of two steps: 1)Apply finite differences in time. 2) Discretize in space with Galerkin-FEM.
More precisely, we employ a one step-θ scheme in time, which allows us to switch between different time-stepping schemes later on by adjusting the parameter θ, see [33].

We begin by uniformly decomposing the time interval $I = [0, T]$ into N_T intervals with time step size $k = \frac{T}{N_T}$ in order to obtain the time discretization:

$$0 = t_0 < t_1 < \cdots < t_{N_T} = T,$$
$$I_n = [t_{n-1}, t_n], \quad t_n - t_{n-1} = k \quad \text{for all } n \in \{1, \ldots, N_T\}.$$

Given a solution $(\widehat{\boldsymbol{v}}^{n-1}, \widehat{\boldsymbol{u}}^{n-1}, \widehat{p}^{n-1})$ at time step t_{n-1}, we calculate the solution of our variational monolithic ALE-FSI system (10) at the next time step by solving

$$\begin{aligned}
&\widehat{\boldsymbol{A}}_\mathrm{T}(\widehat{\boldsymbol{v}}^n, \widehat{\boldsymbol{v}}^{n-1}, \widehat{\boldsymbol{u}}^n, \widehat{\boldsymbol{u}}^{n-1})(\widehat{\boldsymbol{\Phi}}) + k\theta\widehat{\boldsymbol{A}}_\mathrm{I}(\widehat{\boldsymbol{v}}^n, \widehat{\boldsymbol{u}}^n, \widehat{p}^n)(\widehat{\boldsymbol{\Phi}}) \\
&\qquad + k(1-\theta)\widehat{\boldsymbol{A}}_\mathrm{E}(\widehat{\boldsymbol{v}}^{n-1}, \widehat{\boldsymbol{u}}^{n-1}, \widehat{p}^{n-1})(\widehat{\boldsymbol{\Phi}}) = \widehat{\boldsymbol{F}}(\widehat{\boldsymbol{\Phi}}),
\end{aligned}$$

where we collect all terms of $\widehat{\boldsymbol{A}}$ with a time derivative in $\widehat{\boldsymbol{A}}_\mathrm{T}$. On the other hand, $\widehat{\boldsymbol{A}}_\mathrm{I}$ as well as $\widehat{\boldsymbol{A}}_\mathrm{E}$ contain all remaining terms at the current or previous time step respectively.

We showcase this process by two examples and begin by considering the first term of our ALE-FSI problem (9). Therein, we replace the time derivative by a difference

quotient and then multiply with the time step size k. This leads to the following:

$$(\widehat{\rho}_{\mathrm{f}}\widehat{J}\widehat{\partial}_t\widehat{\boldsymbol{v}},\widehat{\boldsymbol{\Phi}}^v)_{\widehat{\Omega}_{\mathrm{f}}} \to (\widehat{\rho}_{\mathrm{f}}\frac{1}{2}(\widehat{J}^n+\widehat{J}^{n-1})(\widehat{\boldsymbol{v}}^n-\widehat{\boldsymbol{v}}^{n-1}),\widehat{\boldsymbol{\Phi}}^v)_{\widehat{\Omega}_{\mathrm{f}}}.$$

Note, that the additional time discretization of $\widehat{J}$ arises as we deal with a non-linear time derivative. As a second illustration, we consider the fifth term of our problem statement (9) containing the solid tensor:

$$(\widehat{\boldsymbol{F}}\widehat{\boldsymbol{\Sigma}}_{\mathrm{s}},\widehat{\nabla}\widehat{\boldsymbol{\Phi}}^v)_{\widehat{\Omega}_{\mathrm{s}}} \to k\theta(\widehat{\boldsymbol{F}}^n\widehat{\boldsymbol{\Sigma}}_{\mathrm{s}}^n,\widehat{\nabla}\widehat{\boldsymbol{\Phi}}^v)_{\widehat{\Omega}_{\mathrm{s}}} + k(1-\theta)(\widehat{\boldsymbol{F}}^{n-1}\widehat{\boldsymbol{\Sigma}}_{\mathrm{s}}^{n-1},\widehat{\nabla}\widehat{\boldsymbol{\Phi}}^v)_{\widehat{\Omega}_{\mathrm{s}}}.$$

This shows how each term is split into an implicit and an explicit part. We remark at this point that the terms resulting from the incompressibility condition, the MMPDE as well as the pressure terms are treated fully implicitly to improve temporal stability [28, p. 284].

Having discretized our system in time, we now turn to the spatial discretization and apply a conforming Galerkin-FEM method. We begin by choosing a spatial mesh for the initial configuration illustrated in Figure 1a and corresponding discrete function spaces for the test and trial functions:

$$\widehat{\mathcal{V}}_{\mathrm{h}}^0 \subset \widehat{\mathcal{V}}^0, \quad \widehat{\mathcal{V}}_{\mathrm{h}}^1 \subset \widehat{\mathcal{V}}^1 \quad \text{and} \quad \widehat{\mathcal{V}}_{\mathrm{h}}^2 \subset L^2(\widehat{\Omega}).$$

Next, we consider basis functions of these finite dimensional spaces, e.g.:

$$B_{\mathrm{h}}^v := \{\widehat{\boldsymbol{\Phi}}_{\mathrm{h},1}^v,\dots,\widehat{\boldsymbol{\Phi}}_{\mathrm{h},m}^v\} \text{ with } \dim\widehat{\mathcal{V}}_{\mathrm{h}}^0 = m \text{ and } \operatorname{span}(B_{\mathrm{h}}^v) = \widehat{\mathcal{V}}_{\mathrm{h}}^0.$$

This allows us to define our discrete solution variables

$$\widehat{\boldsymbol{v}}_{\mathrm{h}}^n \in \widehat{\mathcal{V}}_{\mathrm{h}}^0, \quad \widehat{\boldsymbol{u}}_{\mathrm{h}}^n \in \widehat{\mathcal{V}}_{\mathrm{h}}^1 \quad \text{and} \quad \widehat{p}_{\mathrm{h}}^n \in \widehat{\mathcal{V}}_{\mathrm{h}}^2$$

by writing them as a linear combination of the basis functions, e.g.:

$$\widehat{\boldsymbol{v}}_{\mathrm{h}}^n = \sum_{i=1}^m \hat{v}_{\mathrm{h},i}^n\widehat{\boldsymbol{\Phi}}_{\mathrm{h},i}^v, \quad \hat{v}_{\mathrm{h},i}^n \in \mathbb{R}.$$

As we apply a conforming FEM method, the test functions are chosen from the same function spaces as the trial functions. Moreover, it suffices to consider only the basis functions as test functions since our ALE-FSI system (9) is linear in $(\widehat{\boldsymbol{\Phi}}^v,\widehat{\boldsymbol{\Phi}}^u,\widehat{\Phi}^p)$.

Summing up, we obtain the discretized problem to our abbreviated Variational Monolithic ALE-FSI system (10).

Problem Statement 10 (Discretized Variational Monolithic ALE-FSI Problem)**.** For all time steps $n \in \{1,\dots N_T\}$, find $\widehat{\boldsymbol{v}}_{\mathrm{h}}^n \in \widehat{\mathcal{V}}_{\mathrm{h}}^0$, $\widehat{\boldsymbol{u}}_{\mathrm{h}}^n \in \widehat{\mathcal{V}}_{\mathrm{h}}^1$ and $\widehat{p}_{\mathrm{h}}^n \in \widehat{\mathcal{V}}_{\mathrm{h}}^2$ satisfying the initial conditions $\widehat{\boldsymbol{v}}_{\mathrm{h}}^0 = \widehat{\boldsymbol{v}}^0$ and $\widehat{\boldsymbol{u}}_{\mathrm{h}}^0 = \widehat{\boldsymbol{u}}^0$ such that:

$$\begin{aligned}&\widehat{\boldsymbol{A}}_{\mathrm{T}}(\widehat{\boldsymbol{v}}_{\mathrm{h}}^n,\widehat{\boldsymbol{v}}_{\mathrm{h}}^{n-1},\widehat{\boldsymbol{u}}_{\mathrm{h}}^n,\widehat{\boldsymbol{u}}_{\mathrm{h}}^{n-1})(\widehat{\boldsymbol{\Phi}}_{\mathrm{h}}) + k\theta\widehat{\boldsymbol{A}}_{\mathrm{I}}(\widehat{\boldsymbol{v}}_{\mathrm{h}}^n,\widehat{\boldsymbol{u}}_{\mathrm{h}}^n,\widehat{p}_{\mathrm{h}}^n)(\widehat{\boldsymbol{\Phi}}_{\mathrm{h}})\\ &\quad = \widehat{\boldsymbol{F}}(\widehat{\boldsymbol{\Phi}}_{\mathrm{h}}) - k(1-\theta)\widehat{\boldsymbol{A}}_{\mathrm{E}}(\widehat{\boldsymbol{v}}_{\mathrm{h}}^{n-1},\widehat{\boldsymbol{u}}_{\mathrm{h}}^{n-1},\widehat{p}_{\mathrm{h}}^{n-1})(\widehat{\boldsymbol{\Phi}}_{\mathrm{h}})\end{aligned} \tag{11}$$

for all $\widehat{\boldsymbol{\Phi}}_{\mathrm{h}} \in B_{\mathrm{h}}^v \times B_{\mathrm{h}}^u \times B_{\mathrm{h}}^p$.

This discretized problem is at each time step a system of non-linear equations for the coefficients $\hat{v}_{\mathrm{h},i}^n$, $\hat{u}_{\mathrm{h},i}^n$ and $\hat{p}_{\mathrm{h},i}^n$, which we will now solve by means of a Newton method.

3.2 Linearization – Newton Method

In order to linearize the discretized system (11), we apply a Newton-like method. For simplicity, we redefine the left and right hand side:

$$\begin{aligned}\widehat{\boldsymbol{A}}(\widehat{\boldsymbol{U}}_{\mathrm{h}}^n)(\widehat{\boldsymbol{\Phi}}_{\mathrm{h}}) &:= \widehat{\boldsymbol{A}}_{\mathrm{T}}(\widehat{\boldsymbol{v}}_{\mathrm{h}}^n,\widehat{\boldsymbol{v}}_{\mathrm{h}}^{n-1},\widehat{\boldsymbol{u}}_{\mathrm{h}}^n,\widehat{\boldsymbol{u}}_{\mathrm{h}}^{n-1})(\widehat{\boldsymbol{\Phi}}_{\mathrm{h}}) + k\theta\widehat{\boldsymbol{A}}_{\mathrm{I}}(\widehat{\boldsymbol{v}}_{\mathrm{h}}^n,\widehat{\boldsymbol{u}}_{\mathrm{h}}^n,\widehat{p}_{\mathrm{h}}^n)(\widehat{\boldsymbol{\Phi}}_{\mathrm{h}})\\ \widehat{\boldsymbol{G}}(\widehat{\boldsymbol{\Phi}}_{\mathrm{h}}) &:= \widehat{\boldsymbol{F}}(\widehat{\boldsymbol{\Phi}}_{\mathrm{h}}) - k(1-\theta)\widehat{\boldsymbol{A}}_{\mathrm{E}}(\widehat{\boldsymbol{v}}_{\mathrm{h}}^{n-1},\widehat{\boldsymbol{u}}_{\mathrm{h}}^{n-1},\widehat{p}_{\mathrm{h}}^{n-1})(\widehat{\boldsymbol{\Phi}}_{\mathrm{h}})\end{aligned}$$

where $\widehat{\boldsymbol{U}}_{\mathrm{h}}^n := (\widehat{\boldsymbol{v}}_{\mathrm{h}}^n,\widehat{\boldsymbol{u}}_{\mathrm{h}}^n,\widehat{p}_{\mathrm{h}}^n)$.

So in short, we now consider

$$\widehat{\boldsymbol{A}}(\widehat{\boldsymbol{U}}_{\mathrm{h}}^n)(\widehat{\boldsymbol{\Phi}}_{\mathrm{h}}) = \widehat{\boldsymbol{G}}(\widehat{\boldsymbol{\Phi}}_{\mathrm{h}}), \text{ for all } \widehat{\boldsymbol{\Phi}}_{\mathrm{h}} \in B_{\mathrm{h}}^v \times B_{\mathrm{h}}^u \times B_{\mathrm{h}}^p. \tag{12}$$

The Newton-like method for this problem is defined as follows:
Given an initial solution $\widehat{\boldsymbol{U}}_{\mathrm{h}}^{n,0}$ at the time step n, we solve

$$\begin{aligned}\widehat{\boldsymbol{A}}'(\widehat{\boldsymbol{U}}_{\mathrm{h}}^{n,j})(\delta\widehat{\boldsymbol{U}}_{\mathrm{h}}^{n,j},\widehat{\boldsymbol{\Phi}}_{\mathrm{h}}) &= -\widehat{\boldsymbol{A}}(\widehat{\boldsymbol{U}}_{\mathrm{h}}^{n,j})(\widehat{\boldsymbol{\Phi}}_{\mathrm{h}}) + \widehat{\boldsymbol{G}}(\widehat{\boldsymbol{\Phi}}_{\mathrm{h}}),\\ \widehat{\boldsymbol{U}}_{\mathrm{h}}^{n,j+1} &= \widehat{\boldsymbol{U}}_{\mathrm{h}}^{n,j} + \lambda\delta\widehat{\boldsymbol{U}}_{\mathrm{h}}^{n,j},\end{aligned} \tag{13}$$

for $j = 0,1,\dots$ until the infinity norm of the residual

$$\widehat{\boldsymbol{R}}(\widehat{\boldsymbol{U}}_{\mathrm{h}}^{n,j+1}) := \widehat{\boldsymbol{A}}(\widehat{\boldsymbol{U}}_{\mathrm{h}}^{n,j+1})(\widehat{\boldsymbol{\Phi}}_{\mathrm{h}}) - \widehat{\boldsymbol{G}}(\widehat{\boldsymbol{\Phi}}_{\mathrm{h}})$$

is smaller than a given tolerance or the given maximum number of Newton steps is reached.

Here the directional derivative $\widehat{\boldsymbol{A}}'$ is realized with a Gâteaux derivative and $\lambda \in (0,1]$ is a damping factor resulting from a line search along the newton step. We now consider both in more detail.

The Gâteaux derivative of $\widehat{\boldsymbol{A}}$ reads:

$$\widehat{\boldsymbol{A}}'(\widehat{\boldsymbol{U}}_{\mathrm{h}}^{n,j})(\delta\widehat{\boldsymbol{U}}_{\mathrm{h}}^{n,j},\widehat{\boldsymbol{\Phi}}_{\mathrm{h}}) = \frac{d}{d\varepsilon}\widehat{\boldsymbol{A}}(\widehat{\boldsymbol{U}}_{\mathrm{h}}^{n,j}+\varepsilon\delta\widehat{\boldsymbol{U}}_{\mathrm{h}}^{n,j})(\widehat{\boldsymbol{\Phi}}_{\mathrm{h}})\Big|_{\varepsilon=0}. \tag{14}$$

Using this formula, the directional derivative $\widehat{\boldsymbol{A}}'$ can be directly calculated. Moreover, we derive from the formula that regular differentiation rules such as the product rule for non-linear terms or the chain rule, e.g. for $\widehat{J}^{-1}$, hold in a similar fashion. In order to simplify the derivation, we show some identities for frequently appearing terms.

Theorem 11 (Linearization rules)**.** *With all notations as previously defined and discarding indices for simplicity it holds:*

i) $\widehat{\boldsymbol{F}}'(\delta\widehat{\boldsymbol{u}}) = \widehat{\nabla}\delta\widehat{\boldsymbol{u}}$,

ii) $(\widehat{J}\widehat{\boldsymbol{F}}^{-T})'(\delta\widehat{\boldsymbol{u}}) = \begin{bmatrix}\widehat{\partial}_y\delta\widehat{\boldsymbol{u}}_y & -\widehat{\partial}_x\delta\widehat{\boldsymbol{u}}_y\\ -\widehat{\partial}_y\delta\widehat{\boldsymbol{u}}_x & \widehat{\partial}_x\delta\widehat{\boldsymbol{u}}_x\end{bmatrix}$,

iii) $\widehat{J}'(\delta\widehat{\boldsymbol{u}}) = \widehat{J}tr(\widehat{\boldsymbol{F}}^{-1}\widehat{\nabla}\delta\widehat{\boldsymbol{u}})$,

iv) $(\widehat{\boldsymbol{F}}^{-1})'(\delta\widehat{\boldsymbol{u}}) = \frac{-\widehat{J}'(\delta\widehat{\boldsymbol{u}})}{\widehat{J}^2}\widehat{J}\widehat{\boldsymbol{F}}^{-1} + \frac{1}{\widehat{J}}\begin{bmatrix}\widehat{\partial}_y\delta\widehat{\boldsymbol{u}}_y & -\widehat{\partial}_y\delta\widehat{\boldsymbol{u}}_x\\ -\widehat{\partial}_x\delta\widehat{\boldsymbol{u}}_y & \widehat{\partial}_x\delta\widehat{\boldsymbol{u}}_x\end{bmatrix}$.

Proof. i): This follows from $\widehat{\boldsymbol{F}} = I + \widehat{\nabla}\widehat{\boldsymbol{u}}$ and the formula for the Gâteaux derivative in equation (14).

ii): We obtain this identity from equation (14) and

$$\widehat{J}\widehat{\boldsymbol{F}}^{-T} = \begin{bmatrix} 1+\widehat{\partial}_y\widehat{\boldsymbol{u}}_y & -\widehat{\partial}_x\widehat{\boldsymbol{u}}_y \\ -\widehat{\partial}_y\widehat{\boldsymbol{u}}_x & 1+\widehat{\partial}_x\widehat{\boldsymbol{u}}_x \end{bmatrix}.$$

iii): Apply Jacobi's formula to equation (14).

iv): This holds since:

$$\widehat{\boldsymbol{F}}^{-1} = \frac{1}{\widehat{J}} \begin{bmatrix} 1+\widehat{\partial}_y\widehat{\boldsymbol{u}}_y & -\widehat{\partial}_y\widehat{\boldsymbol{u}}_x \\ -\widehat{\partial}_x\widehat{\boldsymbol{u}}_y & 1+\widehat{\partial}_x\widehat{\boldsymbol{u}}_x \end{bmatrix}.$$

Then the result follows from equation (14) with the product rule and the chain rule for $\widehat{J}^{-1}$. □

We illustrate the linearization by example of the term $\widehat{J}\widehat{\nabla}\widehat{\boldsymbol{v}}\widehat{\boldsymbol{F}}^{-1}\widehat{\boldsymbol{F}}^{-T}$, which is part of the transformed fluid stress tensor $\widehat{J}\boldsymbol{\sigma}_{\mathrm{f}}\widehat{\boldsymbol{F}}^{-T}$. For simplicity, we neglect the indices for time and Newton step as well as the density $\widehat{\rho}_{\mathrm{f}}$ and the kinematic viscosity $\widehat{\nu}_{\mathrm{f}}$ since they are constant. As already stated previously, the product rule known from regular differentiation holds in similar fashion for the Gâteaux derivative. This leads to:

$$\begin{aligned}(\widehat{J}\widehat{\nabla}\widehat{\boldsymbol{v}}\widehat{\boldsymbol{F}}^{-1}\widehat{\boldsymbol{F}}^{-T})'(\delta\widehat{\boldsymbol{U}}) = \widehat{J}(\widehat{\nabla}\widehat{\boldsymbol{v}})'(\delta\widehat{\boldsymbol{v}})\widehat{\boldsymbol{F}}^{-1}\widehat{\boldsymbol{F}}^{-T} + \widehat{J}\widehat{\nabla}\widehat{\boldsymbol{v}}(\widehat{\boldsymbol{F}}^{-1})'(\delta\widehat{\boldsymbol{u}})\widehat{\boldsymbol{F}}^{-T} \\ + \widehat{\nabla}\widehat{\boldsymbol{v}}\widehat{\boldsymbol{F}}^{-1}(\widehat{J}\widehat{\boldsymbol{F}}^{-T})'(\delta\widehat{\boldsymbol{u}}).\end{aligned}$$

We now conclude with $(\widehat{\nabla}\widehat{\boldsymbol{v}})'(\delta\widehat{\boldsymbol{v}}) = \widehat{\nabla}\delta\widehat{\boldsymbol{v}}$ and the linearization rules ii)-iv).

By applying this technique to each term on the left hand side of our discretized system (12), we obtain in each Newton step (13) a system of linear equations for the Newton update $\delta\widehat{\boldsymbol{U}}_{\mathrm{h}}^{n,j}$. This system can be solved using standard solvers.

Having calculated the Newton update, we iteratively choose the damping factor λ such that the updated residual is lower than the residual at the previous Newton step:

With a fixed $\mu \in (0,1)$, we define for $k = 0, 1, \ldots$

$$\lambda := \mu^k$$

until $\widehat{\boldsymbol{R}}(\widehat{\boldsymbol{U}}_{\mathrm{h}}^{n,j} + \lambda\delta\widehat{\boldsymbol{U}}_{\mathrm{h}}^{n,j}) < \widehat{\boldsymbol{R}}(\widehat{\boldsymbol{U}}_{\mathrm{h}}^{n,j})$.

At this point, we have fully discretized and linearized our variational monolithic ALE-FSI problem (9). So we can now perform numerical simulations for the falling elastic ball.

4 Numerical Simulation and Discussion of Results

In this section, we conduct numerical simulations for the falling elastic ball with two different parameter sets. Our code is available open-source, is built using the open-source finite element library deal.II [1, 3] and is a modification of the code written by Wick [37] to the setting at hand.

We choose second-order continuous quadrilateral finite elements, i.e. the Q_2^{c} element, for the velocity $\widehat{\boldsymbol{v}}$ as well as the displacement $\widehat{\boldsymbol{u}}$ and first-order discontinuous quadrilateral finite elements, i.e. the P_1^{dc} element, for the pressure $\widehat{p}$. This combination satisfies the discrete inf-sup (LBB) condition, see [18, Chapter II, Section 3].

In order to obtain unconditional stability in time and reduced numerical dissipation, we apply the shifted Crank-Nicolson scheme [20] for the time discretization, i.e. $\theta = 0.5 + k$, where k is the time step size as defined at the beginning of Section 3.1.

Moreover, we set the constant factor in the control parameter for the fluid mesh motion $\alpha = 1\times10^{-8}$ and the constant gravitational force field acting on both the fluid and the solid: $f_{\mathrm{f}}(x,y,t) = f_{\mathrm{s}}(x,y,t) = (0,-9.81)\ \mathrm{m/s}^2$. In the Newton method, we iterate until the infinity norm of the residual assumes values less than $TOL = 1\times10^{-8}$ and choose $\mu = 0.6$ as the damping factor in the line search.

Finally, we create a mesh, see Figure 1b, for the initial configuration of the falling elastic ball using the open-source finite element mesh generator Gmsh [17] and solve the linear system arising from the discretization and linearization with the direct solver UMFPACK [9]. We remark that the presented domain decomposition might lead to ill-conditioned linear systems in case of large deformations. While a different mesh with refinement in areas influenced by compression could perform better, we find our choice sufficient for the computational examples considered in this work.

All calculations are performed on an Intel Core i7-7700HQ 4-core CPU paired with 8 GB of RAM running under the GNU/Linux operating system.

4.1 Quantities of Interest

In order to compare our results to those found in Frei et al. [15], we consider the metrics defined there, but focus on those quantities of interest that directly describe the movement of the ball.

Specifically, we let t_0 be the time when the center of the ball reaches the height $h_0 = 0.039\,\mathrm{m}$ and t^* be the time relative to t_0 when the minimal distance between the ball and the lower boundary is equal to the diameter of the ball. At the time $t_0 + t^*$ we also calculate v^* as the spatial mean vertical velocity inside the ball.

We describe the contact of the ball to the lower boundary by considering the time relative to t_0 of the first contact t_{cont}, i.e. the time at which the distance between

Table 1 – Physical Parameters as in Frei et al. [15] (set 1), and our second set (set 2).

Set	ν_f	ρ_f	ρ_s	μ_s	λ_s
1	$7.0114 \times 10^{-5}\,m^2/s$	$1141\,kg/m^3$	$1361\,kg/m^3$	20 kPa	80 kPa
2	$7.0114 \times 10^{-6}\,m^2/s$	$1141\,kg/m^3$	$1361\,kg/m^3$	666.711 kPa	10 MPa

the ball and the lower boundary is locally minimal. Although a thin fluid layer always remains between the ball and the lower boundary, we refer in the following to this situation with contact. In addition to the metrics defined in Frei et al. [15], we also determine the distance between the ball and the lower boundary at the time of contact d_{cont}. Moreover, we define the time t_{jump} relative to t_0 where the maximum height h_{jump} is reached during the rebound. The maximum pressure at the bottom center point $(0,0)$ over all time steps is denoted by p_{bc}.

In order to gain insights into the quality of the solution, we monitor the performance of the Newton solver and the mesh deformation by calculating the average number of Newton steps n_{Newton} as well as the minimal value of $\widehat{J}$ over all cells and time steps. We refer to this quantity by J_{min}.

4.2 Comparison to Fully Eulerian computations (Parameter set 1)

In a first numerical experiment, we consider the scenario from Frei et al. [15] and compare the results obtained therein to those resulting from our ALE approach. The specific physical parameters are listed in Table 1. Our observation period is the time interval $I = [0, 0.6]$ and we choose our time step size as $k = 0.001$. In the following, we compare the results for 0,1,2, and 3 global refinements of our mesh (i.e. 1728, 6644, 26052 and 103172 degrees of freedom). Choosing the ball diameter as a characteristic length $L = 0.022$ and the flow velocity as $v = 0.1129$ (v^* for 26052 DoFs in Table 2) we obtain a Reynolds number of $Re = 35.425$. Thus, we operate well within the range of laminar flow and require no further stabilization.

For a first qualitative impression of the ball movement, we illustrate its position and vertical velocity for 26052 degrees of freedom (DoFs) at four critical time steps in Figure 2. We observe initially, for example at $t = 0.262$ (top left), that the ball is falling with an increasing velocity. When it approaches the lower boundary, it is slowed down and comes to a complete stop at $t = 0.459$ (top right). Even in the images a small rebound, which reaches its maximum height at $t = 0.516$ (bottom left), becomes apparent. Following the rebound, the ball descends again and nears an equilibrium state close to the lower boundary until $t = 0.6$ (bottom right), where only negligible movement remains.

So on first sight, our results are in agreement with the physical expectations. We now want to further quantify the movement of the ball and therefore calculate the minimal distance between the ball and the lower boundary for the four refinement levels at each time step. The results with an emphasis on the time interval containing the contact to the lower boundary and the rebound are depicted in Figure 3a.

In the initial falling phase, the distances to the lower boundary for all four refinement levels are in reasonable alignment. When approaching $\widehat{\Gamma}_{bot}$ however, the ball is slowed down significantly earlier on the coarsest mesh, i.e. refinement level 0. Zooming into the time interval $[0.45, 0.6]$, where the ball is the closest to the lower boundary, we also observe the time of contact, i.e. the time when the distance to $\widehat{\Gamma}_{bot}$ assumes a minimum, is significantly later. Moreover, the graph for refinement level 0 reveals no proper rebound. The ball is reflected, but continues to move upwards with decreasing velocity instead of falling again.

On the finest mesh, i.e. refinement level 3, the ball shows similar falling behavior to the coarser meshes, but computations break down at $t = 0.443$ before the ball comes into contact with the lower boundary. Hence, only the results up to this time step are depicted in Figure 3a. We investigate this issue in more detail later on.

For the refinement levels 1 and 2 almost identical movement is observed. In the falling phase the graphs can hardly be distinguished and the difference in the times of contact is of magnitude 10^{-3}. However, the rebound happens slightly later and is marginally higher on level 2 in comparison to level 1. This phenomena also occurs in fully Eulerian computations in Frei et al. [15].

In order to investigate the convergence with respect to the time step size, we focus on the second refinement level, i.e. 26052 DoFs, and perform calculations for four different time steps: $k \in \{0.004, 0.002, 0.001, 0.0005\}$. The initial falling phase is identical across all time step sizes. Therefore, we concentrate on the time interval containing the contact to the lower boundary and the rebound. The distance to the lower boundary at each time step in this interval for all four time step sizes is depicted

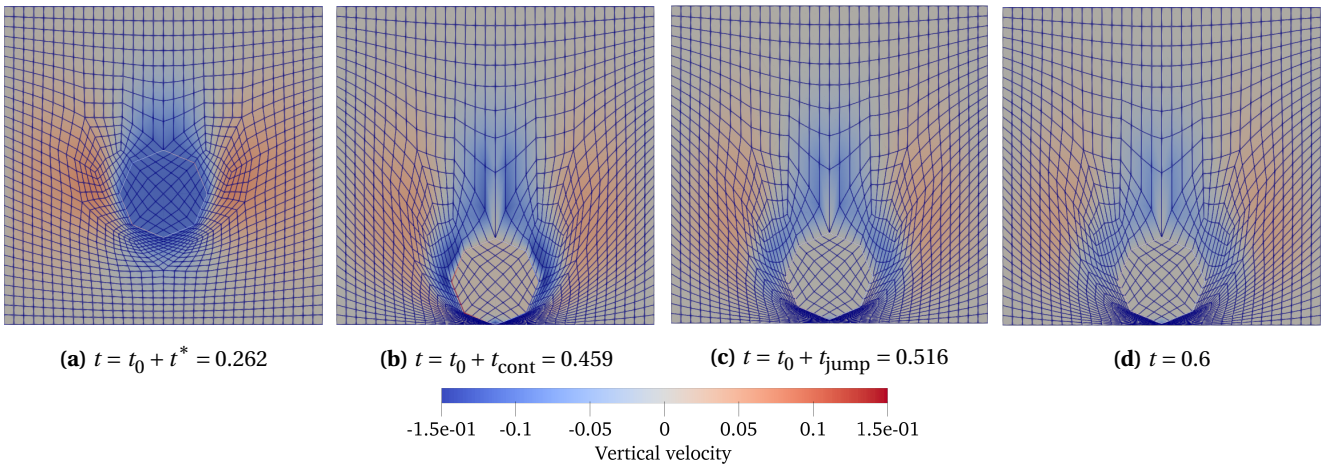

(a) $t = t_0 + t^* = 0.262$ **(b)** $t = t_0 + t_{\text{cont}} = 0.459$ **(c)** $t = t_0 + t_{\text{jump}} = 0.516$ **(d)** $t = 0.6$

Figure 2 – Position and vertical velocity of the ball for 26052 DoFs.

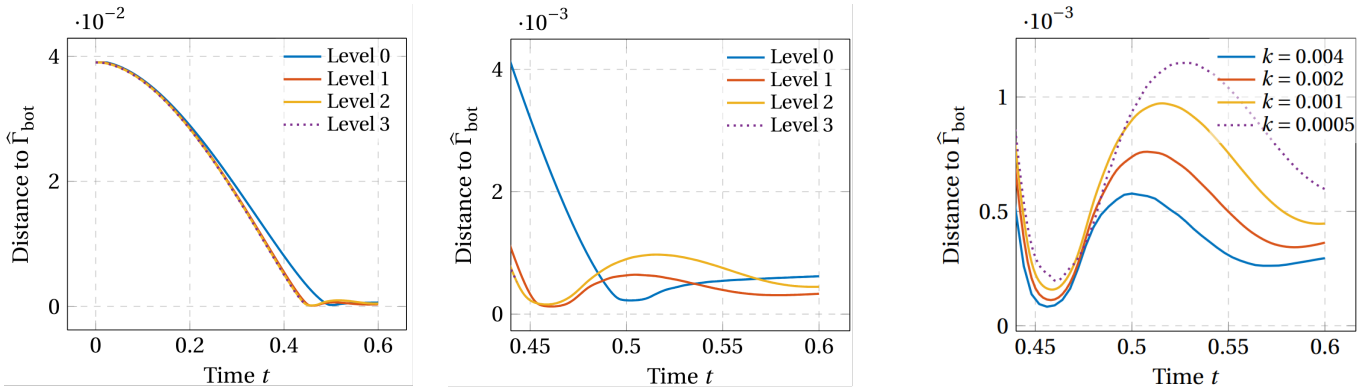

(a) Minimal distances for all four refinement levels.

(b) Time-step study with 26052 DoFs.

Figure 3 – Minimal distances between the ball and $\widehat{\Gamma}_{\text{bot}}$ for the scenario as in Frei et al. [15].

in Figure 3b. We observe that by refining the time discretization, the fluid layer remaining between the ball and the lower boundary at the time of contact becomes thicker. Moreover, the ball rebounds higher for smaller time step sizes. Since we generally associate smaller time step sizes with better solution quality, our findings imply that a larger distance to the lower boundary at the time of contact and a higher rebound describe the movement of the ball more accurately. To this end, further research is required.

Next, we turn to the previously defined quantities of interest. The values obtained in the ALE calculations are listed in Table 2 (ALE 1). For reference, we also display the corresponding values resulting from fully Eulerian calculations in Frei et al. [15] in Table 2 (Eulerian 1).

When comparing the two approaches, we first notice that the deviation for t_0 in all cases apart from the first refinement level (6644 DoFs in Table 2 (ALE 1) is smaller than the ALE time step size of $k = 0.001$. So, up to our chosen accuracy, the values exactly correspond on those levels. For the first refinement level, the value for t_0 obtained with the ALE approach is in alignment with the finer meshes which could indicate a higher precision in comparison to the fully Eulerian results. Overall, the initial movement of the ball appears to be very similar in both calculations.

Considering the metrics t^* and v^* however, we observe that the minimal distance between the ball and the lower boundary is slightly earlier equal to the diameter of the ball with the ALE approach. This phenomena occurs for all refinements apart from the coarsest level, where deviations are expected due to the low resolution of the mesh. At the same time, the average vertical velocity v^* is elevated on all levels in comparison to the fully Eulerian results. This leads to the conclusion that the ball falls faster after the slow initial phase in the ALE calculations. Furthermore, this becomes evident in an earlier time of contact t_{cont} across all refinement levels, while the distance to the lower boundary at contact d_{cont}, although not quantified in Frei et al. [15], is qualitatively in reasonable alignment.

In terms of the rebound, the times t_{jump} only reveal minor differences, whereas h_{jump} is increased for the ALE approach. It remains subject of further research to

Table 2 – Quantities of interest for the first (1) and second (2) parameter set obtained from our ALE approach. For the first set we compare the metrics to the results in Frei et al. [15] calculated therein with a fully Eulerian approach.

DoFs	t_0	t^*	v^*	t_{cont}	d_{cont}	t_{jump}	h_{jump}	p_{bc}	n_{Newton}	J_{min}
Eulerian (1)										
2695	0.2072	0.0623	−0.1021	0.3465	–	–	–	6.7738×10^2	1.1952	–
9928	0.2024	0.0613	−0.1035	0.2738	–	0.3037	0.000203	5.7792×10^2	1.2280	–
37660	0.2038	0.0613	−0.1034	0.2742	–	0.3068	0.000267	5.7504×10^2	1.2496	–
146648	0.2045	0.0615	−0.1030	0.2772	–	0.3053	0.000158	5.7555×10^2	1.3469	–
ALE (1)										
1728	0.208	0.064	−0.1051	0.294	2.2391×10^{-4}	–	–	1.1977×10^3	2.3128	1.0041×10^{-4}
6644	0.204	0.059	−0.1105	0.257	1.2435×10^{-4}	0.301	0.000644	3.4113×10^3	2.3794	1.2698×10^{-4}
26052	0.204	0.058	−0.1129	0.255	1.5803×10^{-4}	0.312	0.000972	5.2180×10^3	2.1298	1.8642×10^{-4}
103172	0.204	0.058	−0.1132	–	–	–	–	1.3172×10^3	2.1081	2.7843×10^{-4}
ALE (2)										
1728	0.191	0.066	−0.0883	0.170	1.6168×10^{-2}	–	–	1.0429×10^3	2.7606	5.6467×10^{-2}
6644	0.179	0.049	−0.1354	0.199	1.0971×10^{-4}	–	–	1.4274×10^5	3.0125	1.2595×10^{-5}
26052	0.177	0.046	−0.1413	0.188	5.6297×10^{-5}	–	–	1.3846×10^5	3.0773	1.7060×10^{-5}
103172	0.177	0.046	−0.1425	0.186	3.9579×10^{-5}	–	–	1.8347×10^5	2.7406	-2.9639×10^{-2}

determine which result describes the real-world behavior of the ball more accurately.

For the maximum pressure at the bottom center point p_{bc} we obtain significantly higher results in the ALE calculation. While the pressure initially assumes values similar to those in the fully Eulerian framework, a sharp increase around the time of contact becomes apparent. This seems reasonable, but at this point the question of which result is more accurate once more remains open.

In both cases, although the small values for J_{min} reveal strong mesh deformations in the ALE approach, the Newton solvers perform excellently. This indicates a high quality of the solutions.

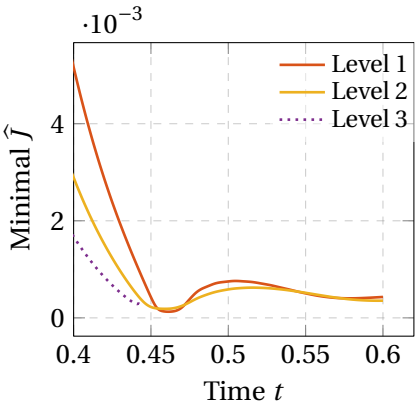

Figure 4 – Minimal values of $\widehat{J}$ over all cells for the scenario as in Frei et al. [15] and the refinement levels 1–3.

Finally, we attempt to explain the breakdown of the calculations on the finest mesh (103 172 DoFs in Table 2 (ALE 1). Therefore, we investigate the mesh deformation and plot the minimal values of $\widehat{J}$ over all cells at each timestep in the critical time interval around the breakdown in Figure 4. For scaling reasons we neglect the coarsest mesh as the mesh deformations are significantly smaller, i.e. $\widehat{J}$ is significantly larger, in this case. We observe that $\widehat{J}$ assumes small values of magnitude 10^{-4} for the third refinement level, which is also the case for the coarser meshes. However, combining this large cell deformation with the already small cell size due to the high resolution on the finest mesh could result in cell volumes that are too small for carrying out computations, hence, leading to the breakdown. While this explanation seems plausible, the observed issue also requires further investigation.

Computational times (CPU time) for our ALE approach in this scenario with the hardware specified at the beginning of the section range from 3 min 9 s on the coarsest mesh to 3 h 28 min on the finest.

4.3 Computational results in a more dynamic scenario (Parameter set 2)

As a second example, we reduce the kinematic viscosity of the fluid in order to increase the dynamics of the system, which also poses larger numerical challenges. The specific physical parameters are listed in Table 1. Choosing again the ball diameter as a characteristic length and the fluid velocity as $v = 0.1413$ (v^* for 26 052 DoFs in Table 2) we obtain a Reynolds number of $Re = 443.36$. Hence, we still operate in the range of laminar flow and can refrain from additional stabilization.

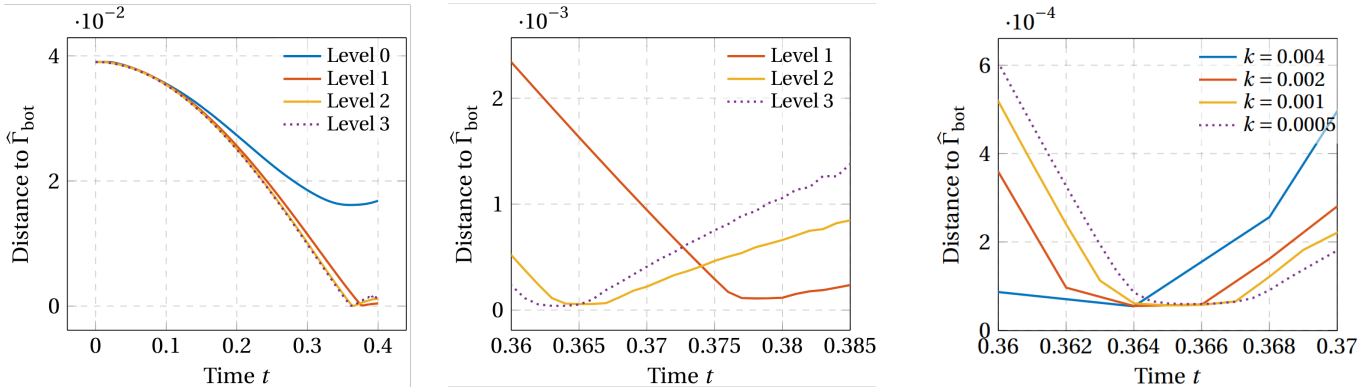

(a) Minimal distances for all four refinement levels.

(b) Time-step study with 26 052 DoFs.

Figure 5 – Minimal distances between the ball and $\widehat{\Gamma}_{\text{bot}}$ for the second scenario.

In addition to those changes, we choose slightly more accurate values for the gravitational forces $f_{\text{f}}(x,y,t) = f_{\text{s}}(x,y,t) = (0,-9.807)\ \text{m/s}^2$ and adjust our observation period to $I = [0,0.4]$. All other parameters remain unchanged. For these calculations, we focus on the initial falling phase of the ball up to the contact and neglect a possible rebound.

We begin by illustrating the minimal distance between the ball and the lower boundary at each timestep for the same four refinement levels in Figure 5a. First of all, it becomes apparent that the movement of the ball on the coarsest mesh deviates significantly from the observations on the finer meshes. The ball is slowed down considerably earlier and comes to a complete stop long before reaching the lower boundary. As already stated previously, this is to be expected due to the low mesh resolution. The results for the remaining three refinement levels are in reasonable alignment. However, zooming into the time interval where the ball is closest to the lower boundary, we notice that contact happens earlier with increasing number of DoFs.

Next, we investigate the convergence with respect to the time step size for this parameter set. Again we focus on the second refinement level with 26 052 DoFs and consider four different time steps: $k \in \{0.004, 0.002, 0.001, 0.0005\}$. Similar to the first scenario, the initial falling phase is identical for all time step sizes. Hence, we direct our attention to the time interval in which the ball comes into contact with the lower boundary. The distance to the lower boundary at each time step in this interval for all four time step sizes is plotted in Figure 5b. We observe that with each refinement of the time discretization the deviation in the results decreases. Therefore, on a qualitative level the solution indeed converges with respect to the time step size. However, for a more rigorous proof of convergence, other quantitative approaches are required.

We remark that in all cases apart from $k = 0.001$ computations break down shortly after the contact. Thus, we neglect the movement of the ball occurring afterwards.

For further quantification, we now turn to the already defined quantities of interest and list them, apart from those describing the rebound, in Table 2 (ALE 2). Neglecting the coarsest mesh with 1728 DoFs, a general observation in comparison to the first scenario is that the ball falls faster. This becomes evident in earlier measured times for t_0, t^* and t_{cont} as well as in increased mean velocities v^*. It is sensible to assume that the significantly lower fluid viscosity in this parameter set is one of the factors leading to the obtained results.

Remarkably, we measure even smaller distances to the lower boundary at the time of contact compared to the first scenario. While with the physical parameters from Frei et al. [15] even on the finest meshes a fluid layer with a thickness of magnitude 10^{-4} remains, we obtain values of magnitude 10^{-5} in this case. As a result, the maximum pressure at the bottom center point is also considerably elevated and the mesh experiences larger deformations as highlighted in the smaller results for J_{min}. On the finest mesh with 103 172 DoFs we even observe negative values for J_{min} shortly after the contact, which indicates negative cell volume and makes no physical sense. Surprisingly, computations do not break down immediately. These findings support the previously raised assumption that the small cell size in combination with large deformations leads to computational problems.

With regard to the average number of Newton steps, the results reveal a slight increase in comparison to the first scenario. The more dynamic movement of the ball appears to increase computational difficulties, nevertheless about 3 Newton steps on average remain in the range of good performance of the solver. Since we observe only minor deviations with increasing mesh res-

olution, we can also in this case assume a high quality of the solution. However, in order to verify their correctness, more calculations with different approaches or real-world experiments are required.

For this parameter set, computational times (CPU time) range from 2 min 12 s on the coarsest mesh to 3 h 55 min on the finest.

5 Summary

In this work, we applied an ALE approach for FSI to the example of the falling elastic ball in a Newtonian fluid. The mesh motion model employs a monitor function with the deformation gradient determinant in the denominator for improved mesh quality. The goal was to show the viability of the presented ALE method in a large deformation setting with contact.

Having completed all the preliminaries, we performed numerical simulations for the falling elastic ball for two different parameter sets and evaluated quantities of interest. As a first example, we considered the physical parameters from Frei et al. [15]. In a qualitative analysis, we found the movement of the ball simulated with our ALE approach to be in agreement with the physical expectations. A more quantitative consideration revealed that the initial falling phase is almost indistinguishable for all four refinement levels. However, the ball is slowed down significantly earlier on the coarsest mesh and does not rebound properly. On the other hand, computations break down on the finest mesh before the ball reaches its lowest point. These numerical difficulties on the finest mesh, common to both scenarios, most likely result from the small cell size in combination with the large mesh deformation. For the refinement levels 1 and 2 the movement of the ball is almost identical.

In a convergence study, we found that with decreasing time step size the fluid layer remaining between the ball and the lower boundary at the time of contact becomes thicker and the height of the rebound increases. Therefore, we assume this behavior to more accurately describe the movement of the ball, while verification of these results is not possible at this point.

When comparing our findings to those obtained in Frei et al. [15] with a fully Eulerian approach, deviations only become apparent in the later falling stages of the ball. In particular, the ball falls faster and rebounds higher in our ALE calculations. Overall the results of both approaches are in reasonable alignment.

In our second computational example, we increased the dynamics of the system by reducing the fluid viscosity. Therein we neglected the rebound and focused only on the movement of the ball up to the contact with the lower boundary. Once more we observed considerable deviations on the coarsest mesh and numerical issues on the finest mesh. In comparison to the first scenario, the ball falls faster and at the time of contact a thinner fluid layer remains between the ball and the lower boundary. Furthermore, a qualitative convergence study showed that the solution indeed converges with respect to the time step size. A quantitative investigation of the convergence is pending.

Both parameter studies exhibited satisfactory performance of the Newton solver which implies a high solution quality. Overall the observations prove the viability of the presented ALE method in a setting with large deformation and contact while producing similar results to a fully Eulerian approach. However, the preceding discussions also reveal that mesh refinement and time step size have to be chosen cautiously.

In ongoing work, specifically Setting 2, is further investigated with other experts (and their codes) in fluid-structure interaction to substantiate the behavior just before, during, and after contact. To date, it is not clear, and future work, whether a plain vanilla ALE-FSI approach such as in the current paper is capable to give accurate results during contact and after contact. Another topic of future investigation will be other constitutive solid laws such as of Neo-Hookean type.

Code Availability: The source code for the results presented in this work can be obtained under `https://github.com/FlorianStahlhuth/FSI-FallingBall` [1].

Acknowledgements: This work was supported by Deutsche Forschungsgemeinschaft (DFG) in the IRTG 2657 "Computational Mechanics Techniques in High Dimensions" with the project number 433082294.

CRediT authorship contribution statement:
F. Stahlhuth: software, formal analysis, writing – original draft; C. Hergl: writing - review & editing; T. Wick: conceptualization, supervision, software, writing - review & editing

References

[1] P. C. Africa, D. Arndt, W. Bangerth, B. Blais, M. Fehling, R. Gassmöller, T. Heister, L. Heltai, S. Kinnewig, M. Kronbichler, M. Maier, P. Munch, M. Schreter, J. Thiele, B. Turcksin, D. Wells, and V. Yushutin. The deal.ii library, version 9.6. *Journal of Numerical Mathematics*, 32:369–380, 2024.

[2] C. Ager, B. Schott, A.-T. Vuong, A. Popp, and W. A. Wall. A consistent approach for fluid-structure-contact interaction based

[1] The precise version used for this publication is permanently stored at `https://archive.softwareheritage.org/swh:1:dir:d3a6e50e6c6c9279fca520f65bdb2ab821b67f69`

on a porous flow model for rough surface contact. *International Journal for Numerical Methods in Engineering*, 119(13): 1345–1378, 2019.

[3] D. Arndt, W. Bangerth, D. Davydov, T. Heister, L. Heltai, M. Kronbichler, M. Maier, J.-P. Pelteret, B. Turcksin, and D. Wells. The deal.ii finite element library: Design, features, and insights. *Computers & Mathematics with Applications*, 81:407–422, 2021. ISSN 0898-1221. Development and Application of Open-source Software for Problems with Numerical PDEs.

[4] M. Astorino, J.-F. Gerbeau, O. Pantz, and K.-F. Traoré. Fluid–structure interaction and multi-body contact: Application to aortic valves. *Computer Methods in Applied Mechanics and Engineering*, 198(45):3603–3612, 2009. ISSN 0045-7825. Models and Methods in Computational Vascular and Cardiovascular Mechanics.

[5] H.-J. Bungartz and M. Schäfer. *Fluid-Structure Interaction: Modelling, Simulation, Optimisation*. Lecture Notes in Computational Science and Engineering. Springer, 2006. ISBN 978-3-540-34595-4.

[6] E. Burman, M. A. Fernández, and S. Frei. A nitsche-based formulation for fluid-structure interactions with contact. *ESAIM: Mathematical Modelling and Numerical Analysis*, 54(2):531–564, 2020.

[7] E. Burman, M. A. Fernández, S. Frei, and F. M. Gerosa. A mechanically consistent model for fluid–structure interactions with contact including seepage. *Computer Methods in Applied Mechanics and Engineering*, 392:114637, 2022. ISSN 0045-7825.

[8] M. Coroneo, L. Yoshihara, and W. A. Wall. Biofilm growth: A multi-scale and coupled fluid-structure interaction and mass transport approach. *Biotechnology and bioengineering*, 111(7): 1385–1395, 2014.

[9] T. A. Davis and I. S. Duff. An unsymmetric-pattern multifrontal method for sparse lu factorization. *SIAM Journal on Matrix Analysis and Applications*, 18(1):140–158, 1997.

[10] J. Donea, S. Giuliani, and J.-P. Halleux. An arbitrary lagrangian-eulerian finite element method for transient dynamic fluid-structure interactions. *Computer methods in applied mechanics and engineering*, 33(1-3):689–723, 1982.

[11] T. Dunne. An eulerian approach to fluid–structure interaction and goal-oriented mesh adaptation. *International journal for numerical methods in fluids*, 51(9-10):1017–1039, 2006.

[12] J. Fara, S. Schwarzacher, and K. Tůma. Geometric re-meshing strategies to simulate contactless rebounds of elastic solids in fluids. *Computer Methods in Applied Mechanics and Engineering*, 422:116824, 2024. ISSN 0045-7825.

[13] M. A. Fernández and J.-F. Gerbeau. *Algorithms for fluid-structure interaction problems*, pages 307–346. MS&A. Springer Milan, Milano, 2009. ISBN 978-88-470-1152-6.

[14] L. Formaggia, A. Quarteroni, and A. Veneziani. *Cardiovascular Mathematics: Modeling and simulation of the circulatory system*. MS&A. Springer-Verlag, Italia, Milano, 2009. ISBN 978-88-470-1151-9.

[15] S. Frei, T. Knoke, M. C. Steinbach, A.-K. Wenske, and T. Wick. Numerical simulations of fully eulerian fluid-structure contact interaction using a ghost-penalty cut finite element approach. *Advances in Computational Science and Engineering*, 3(0):74–94, 2025.

[16] F. M. Gerosa and A. L. Marsden. A mechanically consistent unified formulation for fluid-porous-structure-contact interaction. *Computer Methods in Applied Mechanics and Engineering*, 425:116942, 2024. ISSN 0045-7825.

[17] C. Geuzaine and J.-F. Remacle. Gmsh: A 3-d finite element mesh generator with built-in pre- and post-processing facilities. *International Journal for Numerical Methods in Engineering*, 79:1309 – 1331, 2009.

[18] V. Girault and P.-A. Raviart. *Finite Element Methods for Navier–Stokes Equations: Theory and Algorithms*. Springer Series in Computational Mathematics. Springer-Verlag, Berlin, Heidelberg, 1 edition, 1986. ISBN 978-3-642-61623-5.

[19] R. Glowinski, T.-W. Pan, and J. Periaux. A fictitious domain method for dirichlet problem and applications. *Computer Methods in Applied Mechanics and Engineering*, 111(3-4):283 – 303, 1994. ISSN 0045-7825.

[20] J. G. Heywood and R. Rannacher. Finite-element approximation of the nonstationary navier–stokes problem. part iv: Error analysis for second-order time discretization. *SIAM Journal on Numerical Analysis*, 27(2):353–384, 1990.

[21] J. G. Heywood, R. Rannacher, and S. Turek. Artificial boundaries and flux and pressure conditions for the incompressible navier-stokes equations. *International Journal for Numerical Methods in Fluids*, 22(5):325–352, 1996.

[22] M. Hillairet. Lack of collision between solid bodies in a 2d incompressible viscous flow. *Communications in Partial Differential Equations*, 32(9):1345–1371, 2007.

[23] J. Hron and S. Turek. A monolithic fem/multigrid solver for an ale formulation of fluid-structure interaction with applications in biomechanics. In H.-J. Bungartz and M. Schäfer, editors, *Fluid-Structure Interaction*, pages 146–170, Berlin, Heidelberg, 2006. Springer Berlin Heidelberg.

[24] T. J. R. Hughes, W. K. Liu, and T. K. Zimmermann. Lagrangian-eulerian finite element formulation for incompressible viscous flows. *Computer methods in applied mechanics and engineering*, 29(3):329–349, 1981.

[25] P. Le Tallec and J. Mouro. Fluid structure interaction with large structural displacements. *Computer Methods in Applied Mechanics and Engineering*, 190(24):3039–3067, 2001. ISSN 0045-7825. Advances in Computational Methods for Fluid-Structure Interaction.

[26] C. Peskin. The immersed boundary method. *Acta Numerica*, 11:1–39, 2002.

[27] S. Piperno and C. Farhat. Partitioned procedures for the transient solution of coupled aeroelastic problems – part ii: energy transfer analysis and three-dimensional applications. *Computer Methods in Applied Mechanics and Engineering*, 190(24): 3147–3170, 2001. ISSN 0045-7825. Advances in Computational Methods for Fluid-Structure Interaction.

[28] R. Rannacher. *Methods for Numerical Flow Simulation*, pages 275–332. Birkhäuser Basel, Basel, 2008. ISBN 978-3-7643-7806-6.

[29] T. Richter. *Fluid-structure interactions: models, analysis and finite elements*. Lecture Notes in Computational Science and Engineering. Springer, 2017.

[30] K. Stein, T. Tezduyar, and R. Benney. Mesh moving techniques for fluid-structure interactions with large displacements. *Journal of Applied Mechanics*, 70(1):58–63, 2003. ISSN 0021-8936.

[31] T. Tezduyar and S. Sathe. Modeling of fluid-structure interactions with the space-time finite elements: Solution techniques. *International Journal for Numerical Methods in Fluids*, 54:855–900, 2007.

[32] T. E. Tezduyar, M. Behr, S. Mittal, and A. A. Johnson. Computation of unsteady incompressible flows with the stabilized finite element methods: Space-time formulations, iterative strategies and massively parallel implementations. In *New Methods in Transient Analysis*, American Society of Mechanical Engineers, Pressure Vessels and Piping Division (Publication) PVP, pages 7–24. Publ by ASME, 1992. ISBN 0791810887.

[33] S. Turek. *Efficient solvers for incompressible flow problems an algorithmic and computational approach*. Lecture notes in computational science and engineering 6. Springer, Berlin, 1999. ISBN 354065433X.

[34] S. Turek and J. Hron. Proposal for numerical benchmarking of fluid-structure interaction between an elastic object and laminar incompressible flow. In H.-J. Bungartz and M. Schäfer, editors, *Fluid-Structure Interaction*, pages 371–385, Berlin, Heidelberg, 2006. Springer Berlin Heidelberg. ISBN 978-3-540-34596-1.

[35] H. von Wahl, T. Richter, S. Frei, and T. Hagemeier. Falling balls in a viscous fluid with contact: Comparing numerical simulations with experimental data. *Physics of Fluids*, 33(3): 033304, 2021. ISSN 1070-6631.

[36] W. A. Wall, S. Genkinger, and E. Ramm. A strong coupling partitioned approach for fluid–structure interaction with free surfaces. *Computers & Fluids*, 36(1):169–183, 2007. ISSN 0045-7930. Challenges and Advances in Flow Simulation and Modeling.

[37] T. Wick. Solving monolithic fluid-structure interaction problems in arbitrary lagrangian eulerian coordinates with the deal.ii library. *Archive of Numerical Software*, 1, 2011.

[38] T. Wick. Fluid-structure interactions using different mesh motion techniques. *Computers and Structures*, 89(13-14):1456–1467, 2011.

[39] J. Wloka. *Partial differential equations*. Cambridge University Press, 1987. ISBN 9780521277594.